Tailoring structural and optical properties of Ta2O5 thin films via radio frequency magnetron sputtering for high-refractive index transparent materials

Aïmane Cheikh, Jeremie Gonçalves, Christophe Labbé, Xavier Portier, Philippe Marie, Cedric Frilay, Olivier Debieu, Sylvain Duprey, Wojciech Jadwisienczak, David Ingram, et al.

Journal of Alloys and Compounds 1040 (2025) 183273

Contents lists available at ScienceDirect

Journal of Alloys and Compounds

journal homepage: www.elsevier.com/locate/jalcom

Tailoring structural and optical properties of Ta_2O_5 thin films via radio frequency magnetron sputtering for high-refractive index transparent materials

Aïmane Cheikh [a,*], Jeremie Gonçalves [a], Christophe Labbé [a], Xavier Portier [a], Philippe Marie [a], Cedric Frilay [a], Olivier Debieu [b], Sylvain Duprey [a], Wojciech Jadwisienczak [c], David Ingram [d], Julien Cardin [a]

[a] CIMAP Normandie Université, ENSICAEN, UNICAEN, CEA, UMR CNRS 6252, 6 Boulevard Maréchal Juin, Caen Cedex 4 10450, France
[b] CIRIMAT, Institut Carnot Chimie Balard CIRIMAT, CNRS-INP-UPS, Université Toulouse 3 Paul Sabatier, 118 Route de Narbonne, Toulouse Cedex 9 F-31062, France
[c] School of Electrical Engineering and Computer Science, Ohio University, Athens, OH 45701, USA
[d] Department of Physics and Astronomy, Ohio University, Athens, OH 45701, USA

ARTICLE INFO

Keywords:
Tantalum pentoxide
Magnetron Sputtering
Optical Materials
Refractive index

ABSTRACT

This work investigates the impact of growth conditions, oxygen flow, sputtering power density, and annealing temperature on the optical performance of Ta_2O_5 thin films grown on Silicon (Si) substrate by RF sputtering. The objective is to determine whether the amorphous or crystalline phase provides the optimal trade-off between high refractive index (n), low optical loss (k), and broad optical transparency window (E_{size}). A near-stoichiometric Ta/O ratio of 0.38, close to the ideal 0.40, was achieved at a power density of 3.29 W/cm^2 and oxygen flow of 8 sccm. Crystallization begins at T_A= 650 °C, resulting in a predominant orthorhombic and a minor hexagonal phase as demonstrated by XRD and confirmed by TEM. This crystallization was accompanied by a densification of 7.85 g.cm^{-3} at 750 °C, but showed signs of structural degradation at 850 °C. Ellipsometry shows an increase in n during crystallization to 2.24 at 750 °C, before decreases at 850 °C. The onset of k redshifts from 4 eV to 3 eV, and the optical band gap (E_g) dropped from 4.14 eV to 2.5 eV following crystallization. Transmittance (T), calculated using the transfer matrix method (TMM), showed an average of 80 % over 1–4 eV range for amorphous films and narrowed below 3 eV in crystalline films due to defect-induced mid-gap states. Our findings underscore a critical balance where crystallization enhances the refractive index of Ta_2O_5 thin films at the expense of a restricted transparency window in the NIR-visible range.

1. Introduction

Tantalum pentoxide (Ta_2O_5) films received much interest in advanced technologies owing to their important properties. They are commonly used in a wide range of electronic, optical, and optoelectronic devices such as bandpass interference filters [1], anti-reflection coatings on solar cells [2], corrosion resistance protective coatings [3], optical waveguides material [4,5], or insulator for microelectronic applications such as capacitors [6,7]. Due to their high refractive indexes (n), low extinction coefficient (k) values, giving high transparency window from near-IR to the near-UV, Ta_2O_5 thin films show good compatibility with recent optical functionalities such as advanced structured multilayer waveguide for nonlinear optics applications [8–10].

Ta_2O_5 thin films are synthesized by various growth techniques. But the functional properties of the material strongly depend on the growth technique, substrate, and growth conditions. For instance, Y. Sekido used e-beam evaporation to grow Ta_2O_5 films for implementation as a covering layer of electrodes to maintain high electrochemical energy storage [11]. I. Porqueras et *al.* have reported that the Ta_2O_5, also grown by the e-beam technique, could be implemented as an IR-visible transparent ion conductor active layer in electrochromic applications [12, 13]. Moreover, He et *al.* have used the pulsed laser deposition method to study the impact of growth conditions, in particular, the oxygen pressure on the morphological and optical properties of Ta_2O_5 film [14]. In addition, J.P. Masse et *al.* have studied the effect of annealed temperatures on the optical properties of chemical vapor-deposited Ta_2O_5 films

* Corresponding author.
E-mail address: aimane.cheikh@ensicaen.fr (A. Cheikh).

https://doi.org/10.1016/j.jallcom.2025.183273
Received 25 June 2025; Received in revised form 12 August 2025; Accepted 24 August 2025
Available online 25 August 2025

[15]. It has been reported that Ta_2O_5 film grown by plasma enhanced CVD (PECVD), using organometallic precursors such as $Ta(OC_2H_5)_5$ or $Ta(OCH_3)_5$, contain residual contaminants carbon (C) and hydrogen (H) originating from the incomplete decomposition of precursors during the growth process. Among these various techniques employed for fabricating tantalum oxide, the magnetron sputtering technique is favored to avoid C and H contamination [15,16]. The sputtering method also has the advantage of rapidly producing homogenous films on large substrates by sputtering tantalum target, as requested by the optoelectronic industries. For example, H.J. Quah et *al.* have grown Ta_2O_5 by dual RF magnetron co-sputtering to be integrated into electronics as a passivation layer in MOS-based devices [17]. Zhang et *al.* have used Ta_2O_5 to produce high-performance UV and visible meta-surfaces polarization-independent UV meta-lenses, spin-selective meta-holograms operating in the near UV and blue spectrum and full visible region structural color generating Mie resonators [18].

Most of these studies used silicon wafer substrates due to their ease of integration in microelectronics manufacturing [19,20]. The use of other substrates, such as fused silica and glass, which have an optical transparency window in the visible range, is interesting for colorless optoelectronic devices. While Nb_2O_5 has shown potential for optical thin film applications due to its high refractive index of around 2.30 and minimal optical absorption ($<10^{-4}$) in the visible range [21], Ta_2O_5 stands out as a compelling alternative with a comparable refractive index and significant optical transparency. Ta_2O_5 and Nb_2O_5 are both promising candidates for the aforementioned applications, offering superior chemical resistance and greater thermal stability compared to other high refractive index materials like TiO_2 [15,22].

The refractive index and extinction coefficient of Ta_2O_5 are reported to be dependent on the chemical composition, J.P. Masse et *al.* studied the evolution of the optical and microstructural properties of Ta_2O_5 grown by PECVD and annealed over a broad temperature range up to 900 °C. Using FTIR and SIMS analyses, they showed that increasing the annealing temperature reduces the refractive index by approximately 4 %, from 2.13 to 2.05. This reduction was attributed to carbon desorption in the form of CO_2 or CO, while the optical loss k remained below 10^{-4}. FTIR measurements confirmed this desorption through the disappearance of characteristic peaks in the 1300–1600 cm^{-1} range, associated with bidentate chelating and bridging modes of COO groups bonded to Ta atoms [15]. Meanwhile, Chaneliere et *al.*, in a separate study on Ta_2O_5 grown by CVD, reported that annealing at high temperature 800 °C under O_2 is insufficient to eliminate hydrocarbon contamination, which can be beneficial for optical properties [23].

S. Boughaba et *al.* investigated Ta_2O_5 deposited by PLD under different oxygen pressure. They found that films synthesized under low oxygen pressure (0.14 Pa) were oxygen-deficient and exhibited a high n of around 3.2 with a non-negligible k∼0.4–0.6. In contrast, the injection of oxygen in the PLD chamber (above 2.56 Pa) improved stoichiometry, resulting in n around 2.22 and a significantly reduced absorption (with $k < 10^{-4}$) [24].

Szymanowski et *al.* demonstrated that increasing ion bombardment during PECVD deposition of Ta_2O_5 leads to higher carbon incorporation, which does not degrade the film's optical performance. They further noted that achieving fully oxidized films requires very high oxygen flow rates (100–200 sccm), which yield a refractive index of 2.15 and extremely low optical loss ($k < 10^{-6}$) [25].

Growth conditions alongside annealing treatments under various atmospheres and temperatures can induce crystallization and structural transitions, which in turn affect the material's optical properties, including the refractive index, extinction coefficient, band gap and optical transmittance. Several studies have shown that the low-temperature deposition of Ta_2O_5 favors the formation of the amorphous phase [26,27] while the post-annealing of this latter at temperatures higher than 650 °C promotes the formation of crystalline phases [15,28]. The Ta_2O_5 atomic structure consists of a combination of hexagonal (δ-Ta_2O_5) and orthorhombic (β-Ta_2O_5) phases, with the β-phase becoming predominant at annealing temperatures above 775 °C [23,29,30].

For instance, I. Perez et *al.* investigated the effect of annealing on Ta_2O_5 thin film grown by RF magnetron sputtering and showed that the crystallization occurs above 675 °C, with a structural transition occurring around 750 °C from δ-Ta_2O_5 to β-Ta_2O_5 phase. They mentioned that this structural evolution is accompanied by microstructural changes from flake-like structures on surface to more compact grains, indicating densification and improved crystallinity. A significant widening of the optical band gap from 2.4 eV to 3.8 eV during crystallization, and they specified that the values for δ-Ta_2O_5 are slightly smaller than values for the β-Ta_2O_5 [28]. J.P. Masse et *al.* also identified the same structural transition from δ-Ta_2O_5 to β-Ta_2O_5 between 800 °C and 900 °C, which was accompanied by an increase in n from 2.05 to 2.11. This transition led to a significant rise in absorption ($k > 10^{-4}$), attributed to optical scattering at grain boundaries [15].

Mansour S. Farhan et *al.* achieved crystallization of Ta_2O_5 film into the δ-Ta_2O_5 phase by electron beam evaporation, using ion bombardment with 300 eV oxygen ions. This resulted in a high refractive index of 2.14 larger than that obtained at 400 eV oxygen ions, potentially due to the degrading effect that the higher ion bombardment energy has on the coating refractive index. The enhanced grain size and crystallinity at 300 eV led to a low optical loss ($k = 1.5 \pm 10^{-3}$) [31].

W.J. Liu et *al.* reported that annealing Ta_2O_5 films grown by plasma ion assisted deposition (PIAD) resulted in the formation of nanocrystalline structures within the amorphous matrix, as revealed by high-resolution transmission electron microscope (HRTEM). This microstructural changes contributed to an increase in the refractive index from 2.13 at 325 °C to 2.16 at 425 °C, with a slight increase in the optical loss ($k = 4.5 \pm 10^{-3}$)[32].

W. Ren reported that annealing Ta_2O_5 grown by electron beam evaporation (EBE) on quartz and silicon substrates at 900 °C improves the film's morphology and reduces surface roughness. This crystallization process reduces structural defects, which contributes to enhanced optical transmittance of 82 % over the 1.12–4 eV range for Ta_2O_5/quartz. For Ta_2O_5/Si, the optical band gap increases to 4.46 eV upon annealing at 900 °C, likely due to slight diffusion of silicon into the film, leading to the formation of SiO_2 and tantalum silicate [33]. Cross-sectional high-resolution transmission electron microscopy observations show the presence of a native SiO_2 oxide layer at the Ta_2O_5/Si interface [32,34,35]. Besides, electron energy loss spectroscopy measurements (EELS) made on Ta_2O_5/Si heterostructures depict a Ta/Si inter-diffusion through the interface, with significant diffusion of Ta into the SiO_x interlayer compared to the out-diffusion of Si into Ta_2O_5 [34].

Md. Islam. Sherajul et *al.* demonstrated using density functional theory (DFT) calculations that introducing oxygen vacancies defects in the Ta_2O_5 lattice generates localized mid-gap defect states and shifts the fermi level towards the conduction band. These mid-gap defects act as an intermediate energy level between the valence and the conduction bands, allowing electron excitation across the band gap [36]. Additionally, interlayer oxygen vacancies were found to induce a semiconductor-to-metal transition. Experimentally, Cevro et *al.* reported that the band gap reduces from 4.3 eV for stoichiometric Ta_2O_5 to 4.0 eV in sub-stoichiometric films, and can decrease further to near-zero (0 eV) in the presence of a high density of metallic tantalum aggregates [26].

This study investigates radiofrequency (RF) sputtered Ta_2O_5 thin films and the effects of rapid thermal annealing (RTA), focusing on the amorphous to crystalline phase transition. The objective is to optimize amorphous Ta_2O_5 for high refractive index and low optical losses in the UV–visible-IR range. We primarily investigate the sputtering deposition parameters (sputtering power density and oxygen flow) to determine the optimal growth conditions for achieving a high refractive index close to the bulk value (n_{bulk}=2.02–2.16) with a negligible extinction coefficient ($k < 10^{-4}$), in order to maintain high optical transparency across a broad UV-Visible spectral range. Following growth optimization, the second aspect of this work explores the impact of RTA under a neutral

atmosphere on the structural and optical properties of the Ta_2O_5 layer. We provide a detailed investigation of the relationship between the optical properties of Ta_2O_5 synthesized by sputtering and its chemical and structural characteristics. The film composition was investigated using Rutherford Backscattering Spectroscopy (RBS), while structural properties were examined by means of X-ray diffraction (XRD), Fourier transform infrared spectroscopy (FTIR), and nanoscale properties were characterized thanks to transmission electron microscopy (TEM). We present a robust and versatile method for accurately determining the optical properties of Ta_2O_5 thin films, even on non-transparent substrates such as silicon. This approach combines advanced modeling techniques, using the Transfer Matrix Method, with reliable spectrophotometry data to provide precise optical constants consistent with ellipsometric measurements. This technique not only enables accurate determination of Ta_2O_5 transparency but also offers a practical solution to common challenges in the optical characterization of heterostructures composed of various film materials on non-transparent substrates.

2. Experimental section

Ta_2O_5 films were deposited on double-side polished, (001) oriented, two-inch diameter Boron doped Silicon (Si) substrates using magnetron Radio Frequency (RF) sputtering, for a duration of 1 h. The tantalum (Ta) oxide films were grown by sputtering a three-inch diameter, 99.9 % pure Ta_2O_5 target in a confocal configuration in atmosphere composed of a mixture of argon (Ar) and oxygen (O) atmospheres. In the first series of samples (S_P), the sputtering power density varied at 2.19, 3.28, 4.38, 5.48, and 6.57 W/cm^2, while argon and oxygen flow rates were held constant at 40 sccm and 12 sccm, respectively. In the second series (S_O), the sputtering power density and Ar flow were kept fixed at 3.28 W/cm^2 and 40 sccm, while the oxygen flow increased from 0 to 16 sccm. The effect of annealing was studied using S_A series; the growth conditions were set at 3.28 W/cm^2, Ar flow of 40 sccm and O flow of 8 sccm (refer to Table A1 in supplementary information SI). The rapid thermal annealing treatment after deposition was performed after deposition at temperature (T_A) ranging from 450 °C to 850 °C in 100 °C increments for 2 h, with a temperature ramp of 20 °C/s in neutral atmosphere.

The compositions of the deposited thin film were determined by Rutherford Backscattering Spectroscopy (RBS) at Edwards Accelerator laboratory of Ohio University using a 4.5 MeV tandem accelerator. The samples were positioned at a 7.5° angle to the incoming beam and exposed to a 2.2 MeV ^{4}He ion beam. The energy resolution achieved on the samples ranged from 20 to 30 keV, depending on the investigation depth. RUMP simulation software was employed to analyze the RBS data and calculate the elemental concentrations, which were then used to determine the material density. The density was calculated by dividing the RBS-driven areal mass density (g. cm^{-2}) by the film thickness measured by ellipsometry.

The structural properties of the films were analyzed using a Bruker D8 Discover diffractometer equipped with monochromatic Cu $K_{\alpha1}$ radiation ($\lambda = 1.5406$ Å). The crystal orientation was assessed through grazing incidence X-ray diffraction (GIXRD). All measurements were conducted with an identical optical configuration, including Soller slits set at 2°, a slit width of 1.2 mm, and 1D LYNXEYE detection mode, covering a 20–60° angular range. The measurements were taken with a step size of 0.0198° and a step time of 2 s, resulting in a total scan duration of approximately 2 h. Peak indexation was performed using X'Pert high score plus software to determine the structural details of the tantalum oxide. The films' structure was also investigated by infra-red transmission measurements using a Nicolet IS50 FTIR spectrometer, with a 0° incidence angle and TE-polarized incident wave. The spectra were corrected from interferences fringes and from the Si substrate contribution based on the most intense peak at 624 cm^{-1} corresponding to the Si-C stretching mode of substitutional C in the Si wafer [37].

Nanoscale investigations were conducted using conventional and high-resolution transmission electron microscopy (CTEM and HRTEM) with a double-corrected field emission gun JEOL ARM 200 F, operated at 200 kV and integrated with a scanning setup (STEM). The microscope was also equipped with a CENTURIO energy dispersive X-ray spectrometer (JEOL). Thin (electron transparent) foils for observations were prepared using a dual-beam focused ion beam system (FEI Helios Nanolab 660). Before applying the platinum (Pt) protection required for the Ga beam thinning process, a carbon film of a few tens of nanometers was deposited directly onto the films to distinguish clearly the top of the film. The structural characterization techniques we employ are also fundamental in other advanced manufacturing fields, including solid-state additive manufacturing to investigate the impact of processing conditions on microstructure, hardness, wear and corrosion resistance [38–41].

The film thickness, refractive index (n), extinction coefficient (k) and band gap (E_g) were determined using Horiba Jobin-Yvon UVISEL variable Angle Spectroscopic Ellipsometer (VASE) method, which relies on changes in the polarization state of the incident beam after reflection. The experimental functions Ic and Is, derived from the ellipsometric angles Ψ and Δ, were measured over an energy range of 1.5 eV up to 6 eV at three different incident angles of 65°, 70° and 75°, using a rotating-compensator spectroscopic ellipsometer. These ellipsometric experimental functions Ic and Is were modeled by combining a structural and dispersion model using the Deltapsi2 software. The structural model employed in this study consisted of two layers atop a semi-infinite substrate. The first layer represents the deposited Ta_2O_5 material, while the second layer accounted for surface roughness. The refractive index of the surface roughness layer was described by the Bruggeman effective medium approximation (EMA) model, simulating a mixture of the deposited material and air voids. Based on previous studies of Ta_2O_5 [24,42–45], the single oscillator Tauc-Lorentz (TL) dispersion model was chosen to describe the deposited material and to fit the experimental functions Ic and Is for all samples. This dispersion model incorporates several parameters, including the band gap energy E_g, the oscillator's strength A, the relative permittivity at an infinite energy ε_∞, the energy position of extinction coefficient peak E_0, and the broadening term C.

To investigate the optical transmittance of Ta_2O_5, a few films were grown on fused silica substrates. Visible range spectra were measured using a Perkin Elmer Lambda 1050 UV–visible-NIR dual-beam spectrophotometer. Measurements were conducted at normal incidence with an incident wave polarized in TE mode with a beam size of 5 × 5 mm^2. The optical reflectance Ta_2O_5/Si films were measured using the same spectrophotometer, equipped with a Universal Reflectance Accessory (URA), at an incidence angle of 8° with an incident wave polarized in TE mode and a beam size of 5 × 5 mm^2.

3. Results and discussion

3.1. Structural, microstructural and compositional characterization

The composition of the sputtered tantalum oxide films grown on Si substrates was determined using RBS measurements across samples deposited at various sputtering power densities, oxygen flow rates, and annealing temperatures. Fig. 1 illustrates that the as-deposited film of the S_O series grown without oxygen flow (0 sccm) was found to be low oxygen-deficient, exhibiting a Ta/O ratio of approximately 0.44, compared to the expected stoichiometry of Ta_2O_5 (~0.4). However, the introduction of oxygen flow reduces the Ta/O ratio, yielding a stable mean value of 0.38 regardless of the oxygen flow. S. Boughaba et *al.*, observed that Ta_2O_5 thin films grown by PLD at low oxygen pressure were highly-oxygen-depleted, with a Ta/O ratio between 0.6 and 0.7, while a stable ratio of around 0.38–0.44 could be achieved at higher oxygen flow [24]. The results of our study align with those findings, indicating that higher oxygen flow during growth leads to an increased oxygen content in films limited by Ta_2O_5 stoichiometry. Similarly for S_P, the composition remained consistent with a Ta/O ratio of around 0.38,

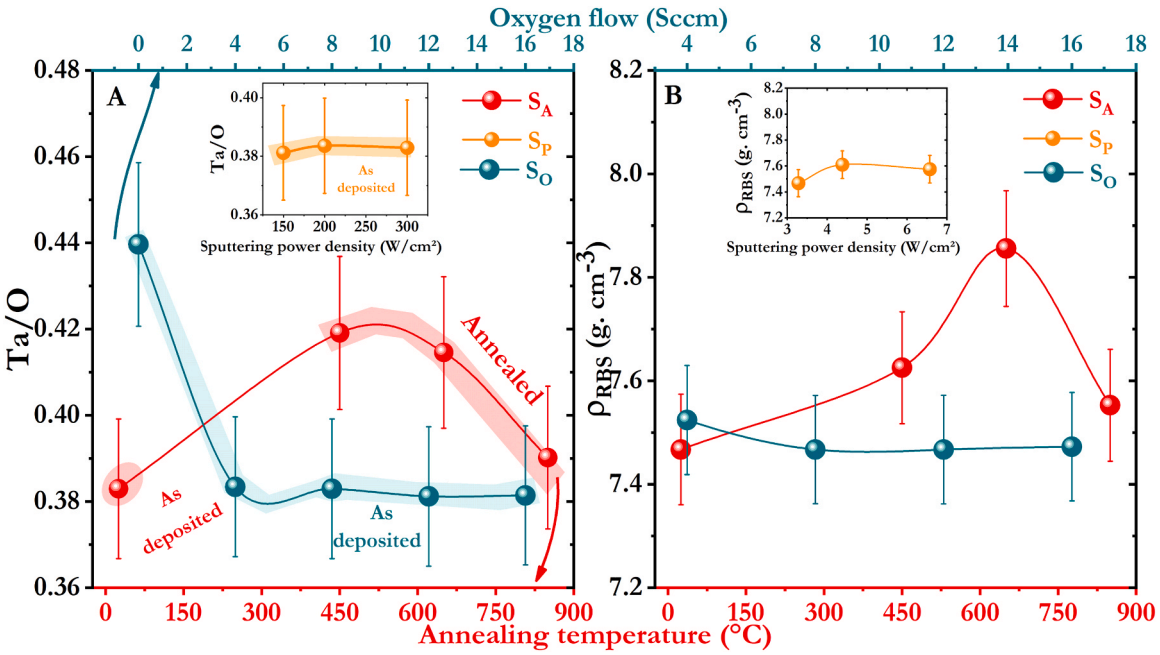

Fig. 1. (A) Variation of the cationic Ta/O ratio with annealing temperature (S_A) and oxygen flow (S_O), with lines included as visual guides. Inset: Ta/O ratio variation as a function of sputtering power density (S_P). (B) Density ρ_{RBS} of Ta_2O_5 as a function of oxygen flow (S_O) and annealing temperature (S_A), with associated error bars. Inset: density as a function of sputtering power density (S_P).

like those grown under varying oxygen flows. For S_A series, the Ta/O ratio peaked at 0.42 at 450 °C and 650 °C, before decreasing to 0.39 at 850 °C. The values obtained in our study demonstrate a consistent and near-stoichiometric Ta_2O_5 composition (Ta/O ~0.4), with a relative variation of 5 %. An increase in the cationic ratio Ta/O from 0.400 to 0.405 was also observed by L. Wang [46], accompanied by a shift in the binding energy of the adsorbed oxygen peak from 532.35 to 532.48 eV in XPS analysis, which is typically associated with oxygen vacancies. This aligns with our findings between 450 °C and 650 °C and may suggest oxygen depletion in our films. Additionally, the films contained a small concentration of Ar, approximately 0.025 %, originating from the sputtering atmosphere. P.H. Chang et *al.* reported an increase in the Ta/O ratio from 0.369 at 600 °C to 0.377 at 1000 °C [47]. The opposite trends observed in the Ta/O ratio arise from differences in oxygen availability, interface behavior, and annealing conditions, as their approach involved direct current (DC) sputtering of a pure Ta target with a 10 s annealing. While, the decrease in the ratio at 850 °C observed in our study indicates a conservation of oxygen. This suggests that oxygen is being retained or less lost in the Ta_2O_5 film. At high temperatures, residual oxygen causes silicon oxidation, leading to the formation of 13 nm thick SiO_2, even under inert conditions (as shown in the TEM section). This thickening of the SiO_2 layer from 3 nm to 13 nm, over the 2 h annealing period, limits oxygen loss by acting as a diffusion barrier and leads to a subsequent reduction in the Ta/O ratio. In contrast to our findings, in the case of Chang's study, the use of a sputtered 35 nm SiO_2 layer that acts as a diffusion barrier, combined with a brief 10 s annealing treatment, effectively limits interfacial oxygen exchange. Alongside a growing atmosphere richer in oxygen (30 % instead of 16 % in our case), the films show a slight increase in the Ta/O ratio with temperature, reflecting moderate oxygen loss without compensation. These differences highlight the critical role of oxygen injected into the chamber, annealing duration, and oxygen dynamics at the interface.

According to the RBS findings, the density (ρ_{RBS}) of Ta_2O_5 has been calculated and presented in Fig. 1(B) as a function of the growth conditions. For S_O, the density decreases from 7.52 g.cm^{-3} as the oxygen flow increases from 4 to 8 sccm, and then stabilizes around 7.46 g.cm^{-3} for oxygen flows between 8 and 16 sccm. With increasing sputtering power density (S_P), no significant variation is observed across different power densities (as can be seen in the inset of Fig. 1(B)). In contrast, for S_A, ρ_{RBS} increases from 7.46 to 7.85 g.cm^{-3} as T_A rises to 650 °C, then decreases to 7.55 g.cm^{-3} for 850 °C. The lower density values compared to the bulk density of 8.2 g.cm^{-3} [48] are due to a less complete crystallization, stemming from a reduced volumetric atomic concentration. However, they are consistent with the densities reported for thin films, ranging from 6 g.cm^{-3} to 7.85 g.cm^{-3} [6,49]. The observed increase in film density from 7.46 at 450 °C to 7.85 g.cm^{-3} at 650 °C, alongside a stable Ta/O ratio of 0.42, highlights a densification process related to the onset of crystallization, as also reported in previous work [50–52]. The consistent Ta/O ratio points to lattice reordering as the main contributor to densification, rather than compositional variations such as oxygen depletion. At 850 °C, we observe a decline in both density to 7.55 g.cm^{-3} and cationic ratio, which could be a signal of an emerging structural degradation. Although the exact mechanisms remain to be confirmed, potential factors include grain enlargement, the emergence of void, and the formation of SiO_2 diffusion barrier. As grains enlarge under high annealing temperature treatment, the reduction in grain boundary area might promote void formation, leading to a less compact structure. This assumption will be further explored through TEM analysis in the subsequent section.

Fig. 2 presents the X-ray diffraction patterns for Ta_2O_5 films annealed at different temperatures. As shown in Fig. 2(A), no significant diffraction peaks were observed for the as-deposited films or those annealed at temperatures up to 550 °C. However, a double-hump feature is visible between $2\theta = 25°$ and 35°, suggests the absence of long-range crystalline order, indicating an amorphous Ta_2O_5 phase for T_A up to 550 °C. At higher T_A (650 °C – 850 °C), several prominent diffraction peaks were detected, starting at 650 °C, pointing to the formation of a polycrystalline Ta_2O_5 phase. This suggests that annealing at 650 °C induces crystallization of Ta_2O_5 on a silicon substrate, consistent with numerous studies [28,33,44,53–55]. The annealed samples exhibit multiple XRD reflections at various positions. A key challenge lies in distinguishing between overlapping phases. The orthorhombic phase (β-Ta_2O_5) shares many reflections with the hexagonal phase (δ-Ta_2O_5), but β-Ta_2O_5 can be identified by additional minor reflections, particularly around 44.75° and 49.75°, as marked by asterisks in Fig. 2(B) [28,56,57]. These supplementary peaks serve as important markers for phase identification. In

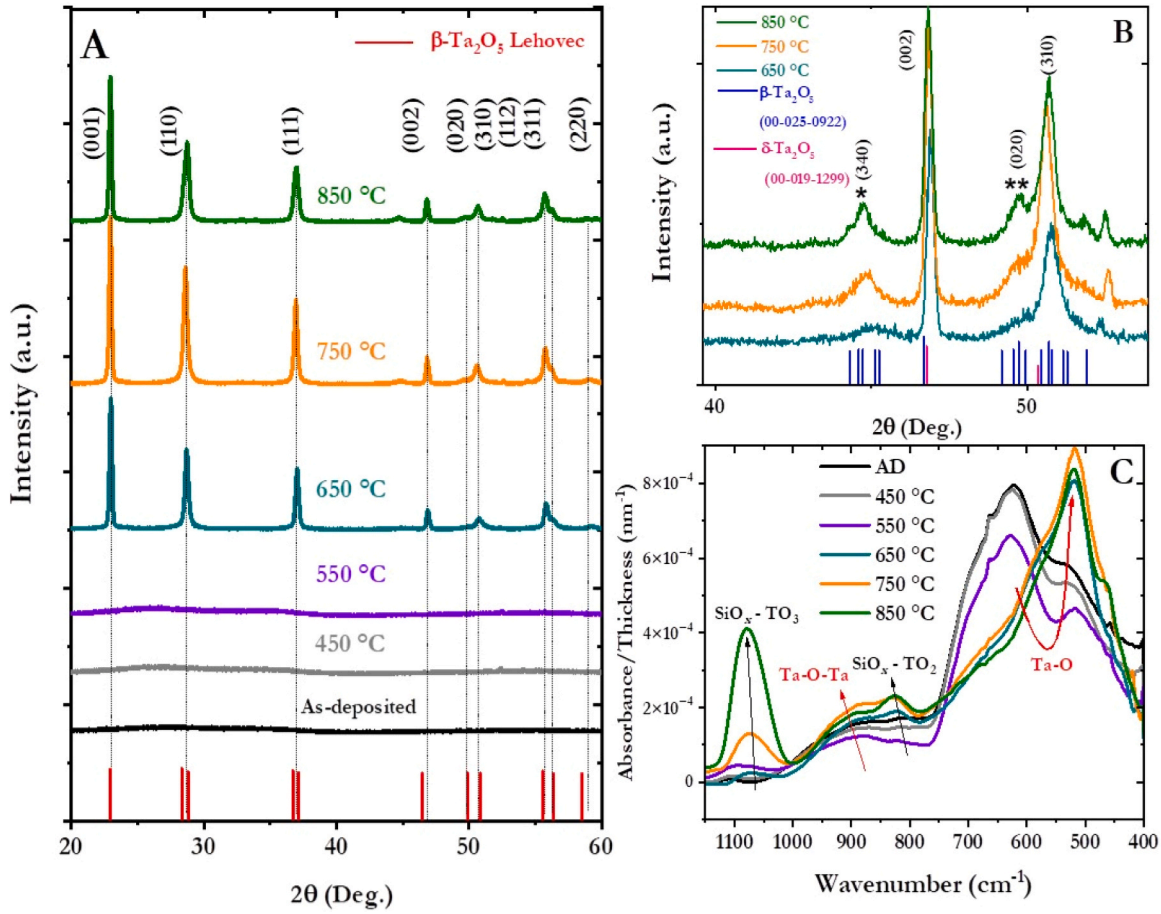

Fig. 2. (A) X-ray diffraction pattern from 20 to 60° with indexed peaks for crystallized Ta_2O_5 thin films and Ta_2O_5 Lehovec reference [58] used for phase identification. (B) Magnified view of the region between 40 and 55°, highlighting minor peaks (*) and (**) essential for phase identification, in comparison to the reference patterns JCPDS files: 00–025–0922 for orthorhombic β-Ta_2O_5 and 00–019–1299 for hexagonal δ-Ta_2O_5 phase. (C) FTIR spectra of Ta_2O_5 films annealed at different temperatures (S_A), measured at normal incidence (0°).

our study, the intensity of these minor reflections increases as T_A rises, suggesting a progressive structural transformation favoring the orthorhombic phase. According to Lehovec [58], the sample annealed at 650 °C exhibits distinct reflections at various 2θ values, corresponding to the (001), (110), (111), (002), (020), (310), (112) and (311) planes. As T_A increases to 850 °C, an increase in the intensity of these minor peaks is observed in Fig. 2(B), underscoring the orthorhombic phase as the primary phase emerging at elevated temperatures. Previous studies have demonstrated that annealing can result in films with two different crystal phases, orthorhombic β-Ta_2O_5 and hexagonal δ-Ta_2O_5, depending on the treatment [28]. J. P. Masse et *al.* [15] showed that Ta_2O_5 films annealed between 600 °C and 800 °C contain both phases, with the orthorhombic phase becoming dominant at temperatures above 900 °C. In our case, the presence of the hexagonal phase in the annealed films appears minimal, and the films are primarily composed of the orthorhombic phase, a conclusion that will be further supported by TEM measurements. Based on the structure reported by Lehovec [58], the observed diffraction peaks correspond to the orthorhombic β-Ta_2O_5 phase, which is the first crystalline structure to form upon annealing. The lattice parameters for this phase are a = 6.29 Å, b = 3.72 Å, and c

Table 1
XRD indexing of annealed Ta_2O_5 films using JCPDS reference patterns for phase identification.

Annealed samples			Reference		JCPD files:			
650(°C)	750(°C)	850(°C)	β-Ta_2O_5 Lehovec [58]		β-Ta_2O_5 00–025–0922		δ-Ta_2O_5 00–019–1299	
2θ (°)			2θ (°)	hkl	2θ (°)	hkl	2θ (°)	hkl
22.96	22.94	22.96	22.96	(011)	22.902	(001)	22.902	(001)
28.68	28.61	28.74	28.32	(110)	28.795	(200)	28.401	(100)
37.04	36.94	36.97	36.71	(111)	-	-	36.806	(101)
45.17	44.88	44.75	-	-	44.74	(340)	-	-
46.89	46.84	46.82	46.47	(002)	46.687	(002)	46.789	(002)
-	49.74	49.75	49.87	(020)	49.728	(0220)	-	-
50.78	50.62	50.68	50.86	(310)	50.705	(2151)	-	-
55.84	55.77	55.72	55.55	(112)	55.77	(0132)	55.66	(102)
-	-	-	-	-	56.291	(3111)	-	-
56.27	56.23	56.32	56.37	(311)	56.328	(2210)	-	-
59.37	59.08	59.03	58.52	(220)	-	-	58.806	(200)

= 7.89 Å, which align with TEM measurements. However, the minor reflection, particularly the peak around 44.75°, could not be identified using the framework proposed by Lehovec [58] (see Fig. 2(B) and Table 1). To resolve this ambiguity, the orthorhombic phase (β-Ta_2O_5) reference pattern (JCPDS file n°: 00–025–0922) identifies the reflection as (340), confirming the orthorhombic phase with lattice parameters a = 6.19 Å, b = 40.29 Å, and c = 3.88 Å, even though it remains undetected by TEM. By comparison, the hexagonal δ-Ta_2O_5 phase pattern reference (JCPDS file n°: 00–019–1299) reproduces the primary diffraction features but fails to account for the minor peaks, particularly those observed at 44.75° and 49.75° (see Fig. 1(B) and Table 1). These findings are corroborated by TEM measurements, which further confirm that the annealed films are primarily composed of the orthorhombic phase.

The angular distribution of the strongest peak remains consistent across all samples, and the full width at half maximum (FWHM) remains unchanged, indicating that the crystallite size is unaffected by T_A. To confirm this, the crystallite size D was estimated using the Scherrer equation (1): $D = K\lambda/\Gamma\cos(\theta)$, where K= 0.9, λ = 1.5406 Å and Γ is the FWHM of the selected peak. The crystallite size was found to be around

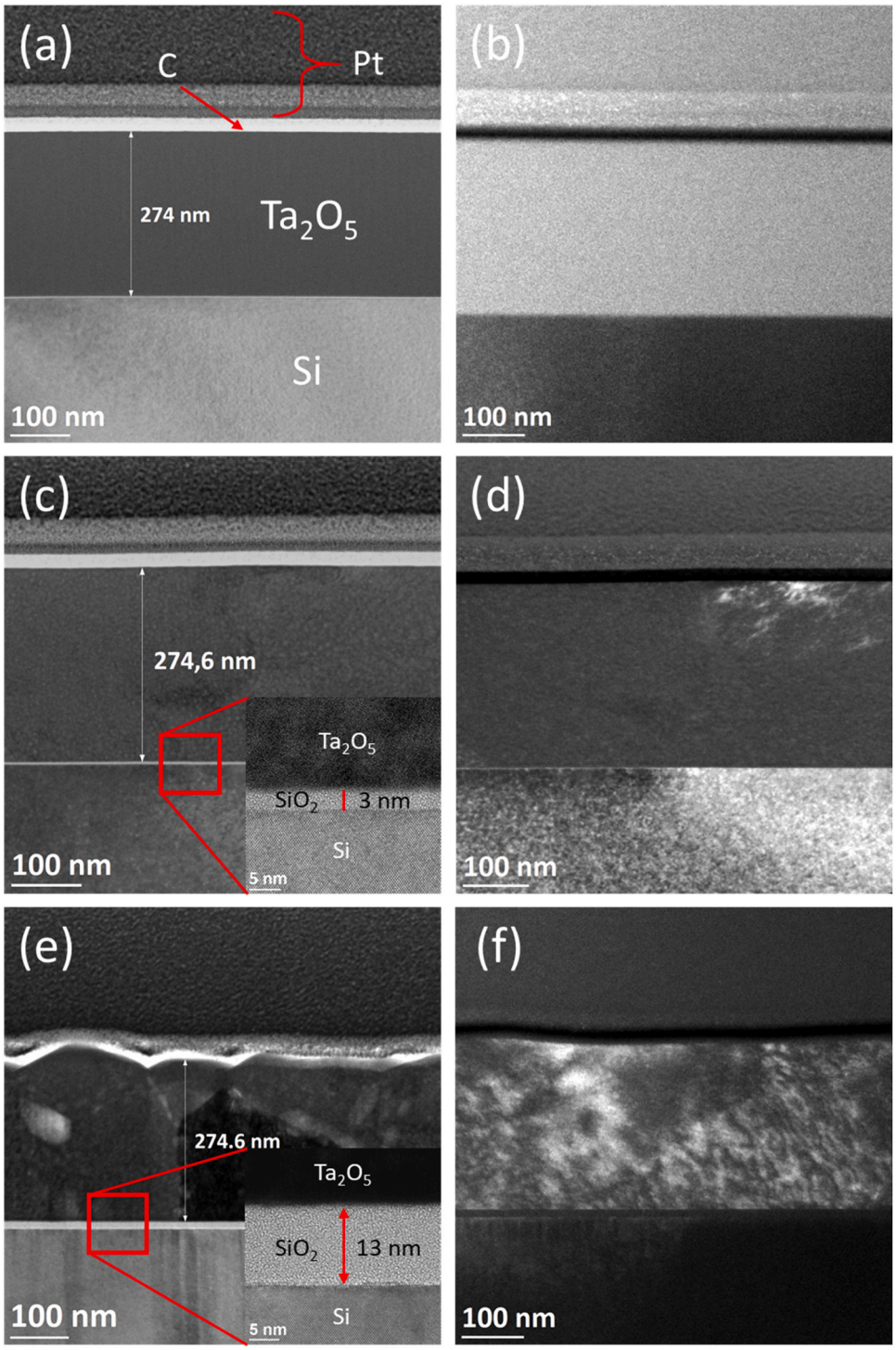

Fig. 3. TEM images of Ta_2O_5 films, grown under 8 sccm and 3.28 $W.cm^{-2}$, annealed at 450 °C, 650 °C and 850 °C. Subfigures (a), (c), and (e) show bright field images, while subfigures (b), (d), and (f) present the corresponding dark field images.

38 nm and did not show significant variation with increasing T_A.

To further explore the changes in vibrational modes in Ta_2O_5 during the annealing treatment, FTIR measurements were performed. According to H. Szymanowski [25], the FTIR spectrum of Ta_2O_5 thin film grown on silicon substrate typically displays three peaks at 518 cm^{-1}, 640 cm^{-1} and 870 cm^{-1}. In our case, for the amorphous Ta_2O_5, *i.e.*, as-deposited and annealed up to 550 °C, a peak is observed at 624 cm^{-1}, which progressively diminishes in intensity as T_A reaches 550 °C. This decrease coincides with the emergence of a peak at 520 cm^{-1}, resulting from a vibrational mode transition to Ta-O stretching in crystalline Ta_2O_5 [25], a trend also observed in reference [14]. A closer examination in the 450–650 cm^{-1} spectral region reveals that the peak shoulder at 520 cm^{-1}, present in the amorphous films, suggests the existence of a minor fraction prearranged or local crystallized Ta_2O_5, a feature beyond XRD detection.

At higher annealing temperature, new distinct mid-infrared peaks emerge at 1080 cm^{-1} and 810 cm^{-1}, associated with the transverse optical phonon modes TO_3 and TO_2 of SiO_x [59]. Their progressive appearance suggests an oxidation of Si substrate, driven by thermal treatment. Up to 550 °C, the position of TO_3 peak remains unchanged but shifts to lower wavenumbers at higher temperature, approaching the value for unstrained, thermally grown SiO_2 at 1078.5 cm^{-1} [60]. According to E. San Andrés et *al.* [60], a similar shift in the TiO_2/Si system is attributed to relaxation within the SiO_2 lattice. The intensification and shift of TO_3 at 850 °C suggest structural changes, potentially linked to oxygen incorporation or relaxation [61], calling for TEM measurements.

TEM investigations were conducted on Ta_2O_5 films annealed at 450 °C, 650 °C, and 850 °C. Fig. 3 presents the cross-sectional TEM images of the annealed Ta_2O_5 films on Si substrates in both bright- and dark-field modes. A 274 nm thick Ta_2O_5 layer was deposited on a thin native amorphous SiO_2 layer, and the underlying Si substrate is visible. The TEM images of the sample annealed at 450 °C (Fig. 3(a) and (b)) show no Bragg contrast, confirming the amorphous nature of the film already observed by XRD measurements. At 650 °C (Fig. 3(c) and (d)), a mixture of amorphous and crystalline regions is observed, indicating the onset of crystallization, consistent with XRD data and FTIR analysis. At 850 °C (Fig. 3(e) and (f)), the Ta_2O_5 film is fully crystallized, with the dark-field image revealing contrast fluctuations due to slight variations in crystalline orientation within grains. The XRD-estimated grain size (38 nm) differs from the larger grains (~200 nm) observed via TEM, which also revealed voids (~50 nm) in the film. Additionally, as illustrated in Fig. 3(c) and (e), the SiO_2 layer thickness increased from 3 nm at 650 °C to 13 nm at 850 °C, aligning with the enhancement of SiO_x-related FTIR peaks and suggesting oxygen incorporation. Fig. 4(a) and (b) depict HRTEM images of the same films annealed at 650 °C and 850 °C, respectively. The HRTEM images of 450 °C annealed film that confirmed it amorphous nature is not shown here. Both images verify the orthorhombic structure of Ta_2O_5. In each case are shown typical examples of grains oriented along the [10–1] direction of the Ta_2O_5 phase. Some regions remain amorphous at 650 °C and no evidence of hexagonal Ta_2O_5 at either temperature.

Fig. 5(a) and (d) present STEM EDX images of crystallized Ta_2O_5 films annealed at 650 °C and 850 °C, respectively, with the corresponding elemental maps for Ta and O shown in Fig. 5(b) and (c) for 650 °C, and in Fig. 5(e) and (f) for 850 °C. The uniform distribution of tantalum and oxygen in the films indicates good compositional homogeneity. However, dark contrasts observed in Fig. 5(d) at 850 °C confirm the presence of voids, as noted earlier. Additionally, Fig. 5(b) highlights a slightly higher oxygen concentration at the bottom of the film annealed at 650 °C (75 at%, Ta/O=0.31) compared to the top (71 at%, Ta/O=0.41), while the oxygen distribution is more uniform at 850 °C (73 at%, Ta/O=0.39), aside from the voids. The ratio at the top of the film, as determined by TEM, matches the values obtained from RBS measurements (Ta/O=0.415 at 650 °C and 0.380 at 850 °C). In parallel, the increase of oxygen content near the film/substrate interface reflects oxygen migration, resulting in the SiO_2 layer thickening from 3 nm up to 13 nm after annealing at 850 °C.

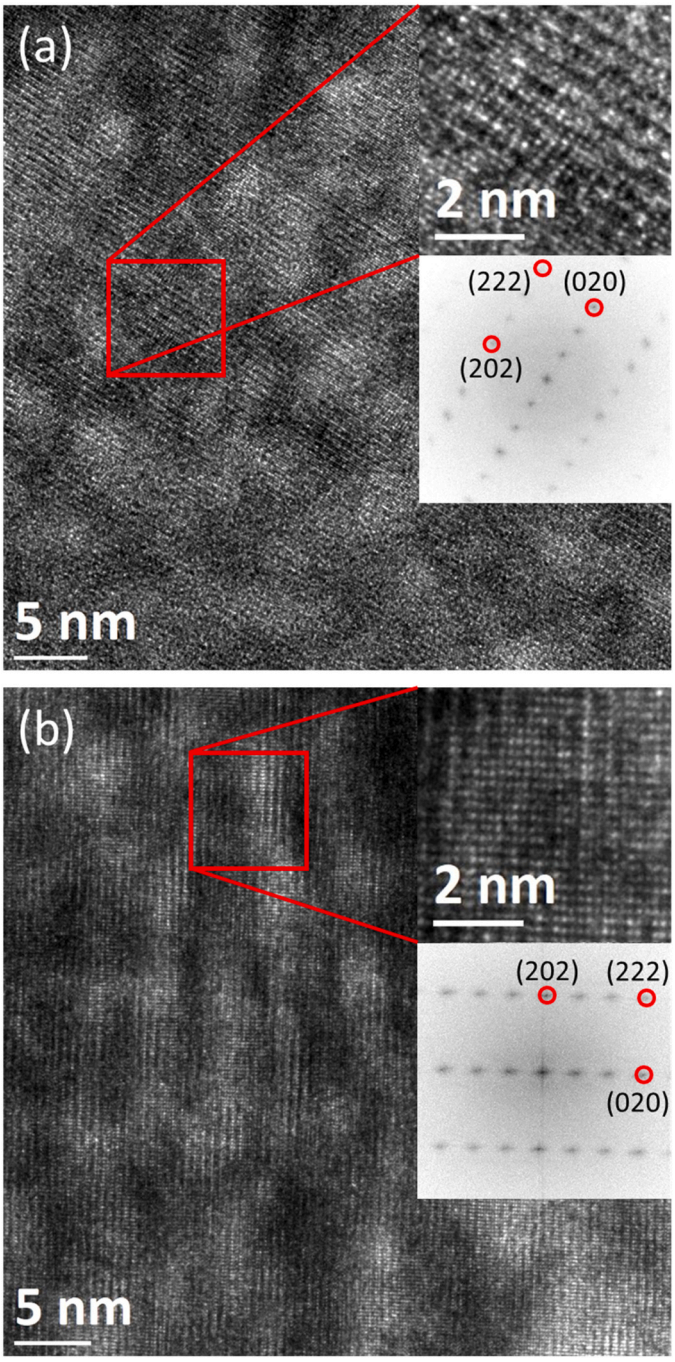

Fig. 4. HRTEM images of Ta_2O_5 films annealed at 650°C (a) and 850°C (b). Insets provide magnified views of well-oriented crystalline regions and their corresponding Fast Fourier Transform (FFTs) patterns, confirming a [10–1] orientation of the orthorhombic structure of tantalum oxide in both samples.

3.2. Ellipsometric and spectrophotometry optical analysis

The refractive index (n) and extinction coefficient (k), key parameters for characterizing linear optical materials, were examined using spectroscopic ellipsometry and reflectometry on Ta_2O_5 films deposited on Si substrate under varying sputtering power densities, oxygen flow rates, and annealing temperatures. Ellipsometric data, represented by the Ic and Is functions, were collected at three incident angles (65°, 70°, and 75°) over a 1–6 eV spectral range, as shown for the as-deposited film

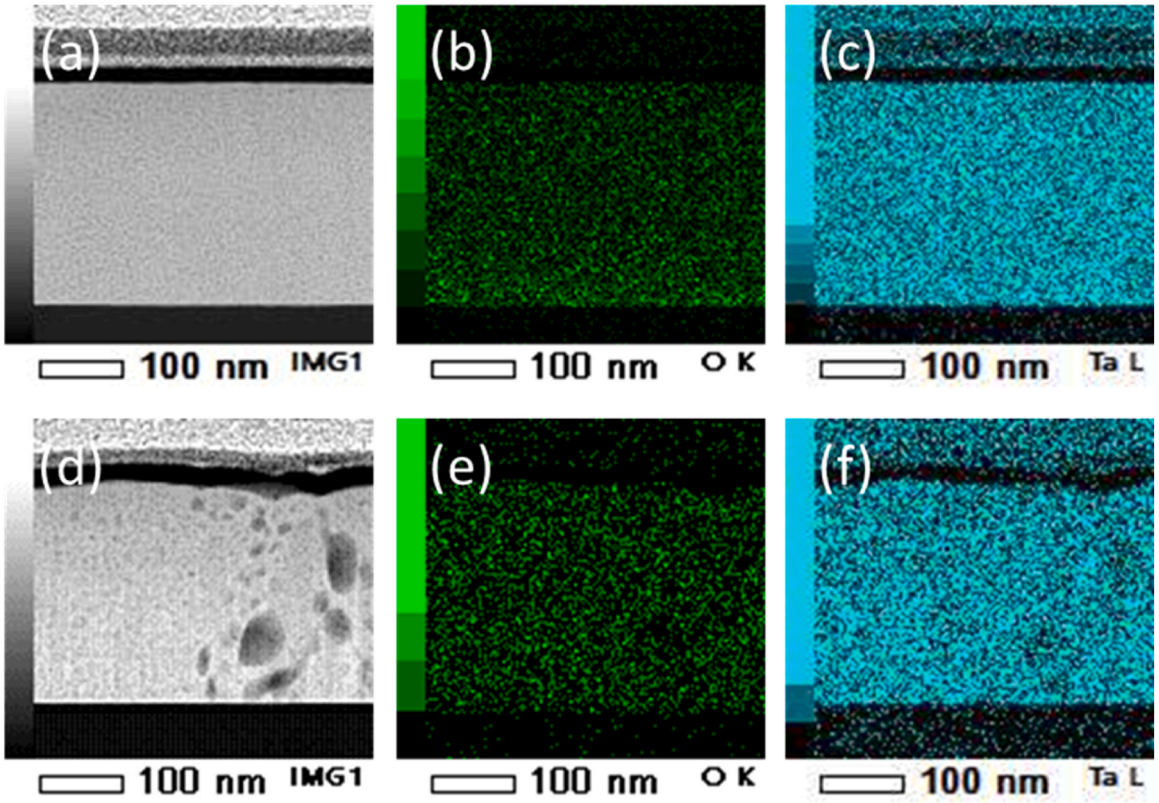

Fig. 5. (a) (d) STEM EDX and (b-f) STEM HAADF images of the Ta_2O_5 film annealed at 650°C and 850°C, respectively, with the corresponding elemental maps of (b, e) oxygen and (c, f) tantalum.

of the S_A series in Fig. 6(A). The values of n and k were obtained using fitting parameters based on the Tauc-Lorentz (TL) model and film thickness. For modeling the amorphous Ta_2O_5 films on silicon, the structure was treated as a homogeneous layer with an additional ~3 nm thick roughness layer, represented by a mixture of Ta_2O_5 and air voids using the effective medium approximation (EMA).

The complex refractive index ($\tilde{n} = n + ik$) was also analyzed using optical reflectance measurements with a Universal Reflectance Accessory (URA), as a complementary technique to Variable Angle Spectroscopic Ellipsometry (VASE). While VASE determines the refractive index and extinction coefficient through polarization rotation, URA measures variations in light intensity, providing a means to validate the VASE results. This comparison was carried out on a sample to confirm the accuracy of VASE for analyzing all samples.

The reflectivity spectra obtained from URA were fitted using a genetic algorithm combined with the simplex method [62], employing the Transfer Matrix Method (TMM) and Tauc-Lorentz dielectric modeling. The TL model parameters derived from both ellipsometry and the fitted URA measurements are summarized in Table A2 (see SI). Fig. 6(B) shows the experimental reflectivity of a Ta_2O_5/Si sample (pink dotted line) compared to the fitted result (black line). The fitted parameters were then used to calculate theoretical values for n and k, with uncertainties. Fig. 6(C) displays the n and k values obtained from both ellipsometry and the fitted reflectivity spectrum, along with their associated uncertainties. Uncertainties in n and k values were determined using a Monte Carlo resampling method, a statistical approach [62]. Based on the parameter uncertainties derived from the TL dispersion model provided by the DeltaPsi2 software, an N-sized population of randomly generated optical indices and extinction coefficients was created. These distributions were rigorously evaluated for conformity to a Gaussian distribution using student's t-tests and skewness assessments and statistically analyzed to provide the mean values of n and k, along with their standard deviations (σ). Assuming Gaussian distribution properties, the uncertainties associated with n and k were each taken as 2σ. This approach demonstrates that the TL model accurately describes the optical behavior of Ta_2O_5 films, with strong agreement between results obtained from both VASE and URA methods, confirming the reliability of the analysis.

Figures SI-1(A) and (C) illustrate the evolution of n and k of the S_p series. Except for the film grown at 2.19 W/cm^2, where Ic and Is functions fitting issues suggest a potential quality or compositional deviations, all other samples exhibit a similar trend in both n and k. Our optical results closely align with the results reported by J. Masse et *al.* [15], with values in the visible and UV regions consistent with other studies [63], particularly for amorphous Ta_2O_5 grown via RF sputtering [42]. The n exhibits a sharp peak around 5 eV, while the k peaks at 6 eV, both associated with strong absorption near the band gap energy of Ta_2O_5. For higher sputtering power densities (3.28 W/cm^2 to 6.57 W/cm^2), k remains negligible in the 1-4 eV range, rising to a maximum around 6 eV. However, for the film grown at 2.19 W/cm^2, both n and k deviate significantly, with k showing higher absorption between 1 and 3 eV. This difference in optical properties between the low and higher power densities results from a pronounced stoichiometric imbalance in Ta_2O_5, suggesting that low power density does not produce pure Ta_2O_5. In addition, the band gap values obtained using the TL model, stabilized around 4 eV as the sputtering power density increased from 3.28 to 6.57 W/cm (refer to Table A1 in SI). However, a different behavior was observed compared to previous studies. For instance, X. Chen et *al.* [42] reported an increase in E_g with sputtering power density, which they attributed to variations in the bonding between oxygen and tantalum atoms.

The refractive index at 2 eV ($n_{2\ eV}$), chosen due to the negligible k, and the Ta_2O_5 film thickness, is presented in Figure SI-2(A). Considering the calculated error bars, n remains constant around 2.14, as the sputtering power increases up to 6.57 W/cm^2. Meanwhile, the Ta_2O_5 thickness increases monotonically, confirming its chemical stability, as

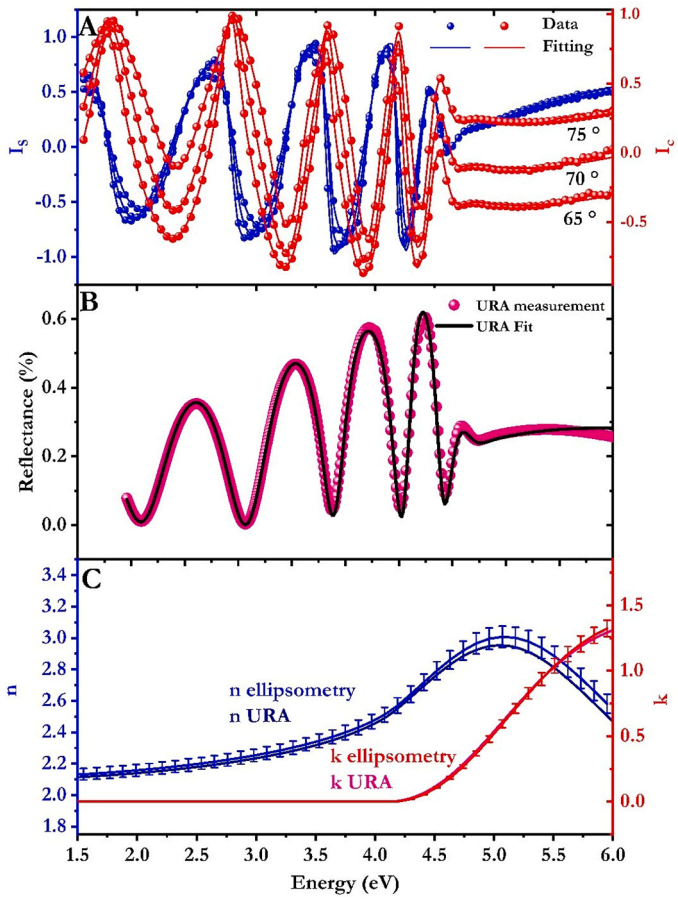

Fig. 6. (A) Measured Is and Ic spectra, derived from the ellipsometric angles Ψ and Δ, using VASE at three different incident angles (65, 70 and 75°) of the as-deposited Ta_2O_5 film belonging to the S_A series, the measured data appears as blue and red points with the TL model fits following as smooth lines obtained using DeltaPsi2 software. (B) Optical reflectance recorded at an 8° incidence angle in TE polarization: The pink dotted line represents the measured data from URA, while the black line corresponds to the fit obtained using the TL model. (C) The refractive index (n) and the extinction coefficient (k) derived from VASE measurements and calculated from URA reflectivity data, along with associated uncertainties.

observed in RBS measurements. A similar trend was reported in another study where n showed minimal variation, while the thickness increased with power density [42,64]. This is expected because, under constant Ar pressure, increasing sputtering power raises the kinetic energy of the particles sputtered from the target, leading to increased film thickness [42]. Additionally, the extinction coefficient at 6 eV ($k_{6\ eV}$) remains stable around 1.40, without any significant changes as a function of sputtering power density (see Figure SI-2(C)).

Figures SI-1(B) and (D) illustrate the n and k spectra of the S_O series. The evolution of n and k follows a similar trend to that observed in the S_P series. However, the ellipsometry measurements reveal that Ta_2O_5 grown under 0 sccm oxygen flow displays significantly different optical properties compared to those grown with oxygen flow (see Figure SI-1 (B)). In contrast, R. Shakoury [65] showed that Ta_2O_5 grown without oxygen (0 sccm) exhibited similar optical characteristics to those grown at low oxygen flow rates of 1 and 2 sccm. In Figures SI-2(B) and (D), the $n_{2\ eV}$ reaches 2.15, while the $k_{6\ eV}$ reaches a maximum under 12 sccm of oxygen flow. S. Boughaba *et al.* [24] reported a similar decrease in the refractive index for Ta_2O_5/Si films deposited by pulsed laser deposition (PLD) with increasing oxygen pressure, stabilizing around 2.15–2.18, which was attributed to highly dense Ta_2O_5 films. H. Szymanowski *et al.* [25] found a similar trend in PECVD-grown samples, noting that high oxygen flow is essential for fully oxidized Ta_2O_5 deposition. Despite the variations in oxygen flow, the band gap E_g remains stable, ranging between 4.04 eV and 4.15 eV (see Table A1 in SI), while L. Wang et *al.* observed a decline from 4.20 to 4.14 eV between 25 and 35 sccm, linked to increased oxygen vacancies and stoichiometric deviation in Ta_2O_5 films [46]. The Ta_2O_5 film thickness decreases by 60 %, from 326 nm to 192 nm, as the oxygen flow increases from 4 sccm to 16 sccm (Figure. SI-2(B)). This reduction is explained by the shorter mean free path of sputtered particles as oxygen ions in the chamber increase, leading to a lower deposition rate and thinner films [66].

The study conducted on the initial two series successfully identified the optimal growth conditions to initiate the investigation of annealing treatment. The sputtering power density was increased to 3.28 W/cm^2 from 2.19 W/cm^2 to avoid suspected variation in Ta_2O_5's composition, which was evident at lower sputtering power. In parallel, the oxygen flow was fixed at 8 sccm to maintain stoichiometric Ta_2O_5 and prevent excessive absorption, which increases at higher oxygen flow, such as 12 sccm. VASE ellipsometry measurements were performed on the as-deposited and annealed Ta_2O_5 films at various temperatures. Ellipsometric data fitting for films annealed between 650 °C and 850 °C was performed without including surface roughness. Fig. 7 (A) and (B) show n and k spectra of the as-deposited and annealed Ta_2O_5 up to 550 °C, including estimated error bars. These curves are similar to those observed in the initial two series (S_P and S_O). However, the spectra of films annealed above 650 °C in Fig. 7 (C) and (D), show notable differences compared to the as-deposited and annealed below 650 °C. Between 650 °C and 850 °C, the maximum of n blueshifts, while the k onset redshifts from 4 eV to 3 eV. These shifts may result from chemical or structural changes induced by the annealing process. Although stoichiometry deviates by 5 %, this is insufficient to account for the significant changes in n and k. However, XRD, FTIR, and TEM measurements revealed a notable structural transformation from amorphous to orthorhombic phase after annealing at 650 °C. This crystallization induces a redshift in k onset and reflects changes in the electronic structure, affecting the E_g energy and the optical response of Ta_2O_5.

The $n_{2\ eV}$ increases with temperature, reaching a maximum at 750 °C before dropping to 2.18 at 850 °C (see Fig. 8(A)). This tendency mirrors the RBS-derived density variation (Fig. 1(B)). The increase in $n_{2\ eV}$ and concurrent thickness reduction between 650 °C and 750 °C suggest densification during crystallization, as confirmed by XRD. Beyond 750 °C, the opposite tendency reflects a degradation of density in the crystalline phase, as supported by TEM measurements. Additionally, an increase in $k_{6\ eV}$ is observed from 1.38 to 1.61 between 450 °C and 650 °C, accompanied by a redshift in the k onset (see Fig. 8(B)). These behaviors point to enhanced absorption caused by electronic structure changes during densification. Above 750 °C, the non-monotonic behavior of $k_{6\ eV}$ reflects perturbations in the electronic properties, consistent with the observed drop in density (Fig. 1(B)).

The evolution of density (ρ_{LL}) was further supported by the Lorentz-Lorentz Law expressed by the following equation (2): $\rho_{LL} = \frac{3}{4\pi}\frac{M_{Ta2O5}}{\alpha N_A}\left(\frac{n_{2eV}^2-1}{n_{2eV}^2+1}\right)$, where α is the molecular electronic polarizability, Na is Avogadro's constant, M is the Ta_2O_5 molar mass (equal to 441.89 g.mol^{-1}) and $n_{2\ eV}$ is the refractive index at 2 eV, respectively. The global molecular electronic polarizability of Ta_2O_5 is expressed as the sum of electronic polarizability of the corresponding ions Ta^{5+} and O^{2-} as $\alpha = A\ \alpha_{Ta5+} + B\ \alpha_{O2-}$, where A and B are the stoichiometric factors, and α_{Ta5+} and α_{O2-} are the electronic polarizabilities of Ta^{5+} and O^{2-}, respectively. These latter were found in the literature to be equal to $\alpha_{Ta5+} = 2.82 \pm 10^{-24}$ cm^3 and $\alpha_{O2-} = 2.40 \pm 10^{-24}$ cm^3, and the molecular electronic polarizability of Ta_2O_5 is found to be $\alpha = 1.76 \pm 10^{-23}$ cm^3. Based on the obtained α value, ρ_{LL} remains in the range of 6.36–6.63 g.cm^{-3}, which is approximately 74 % of the bulk density (8.72 g.cm^{-3}). The ρ_{LL} values are lower by one factor than ρ_{RBS} potentially attributed to the α value, a parameter that has not been extensively investigated in the literature.

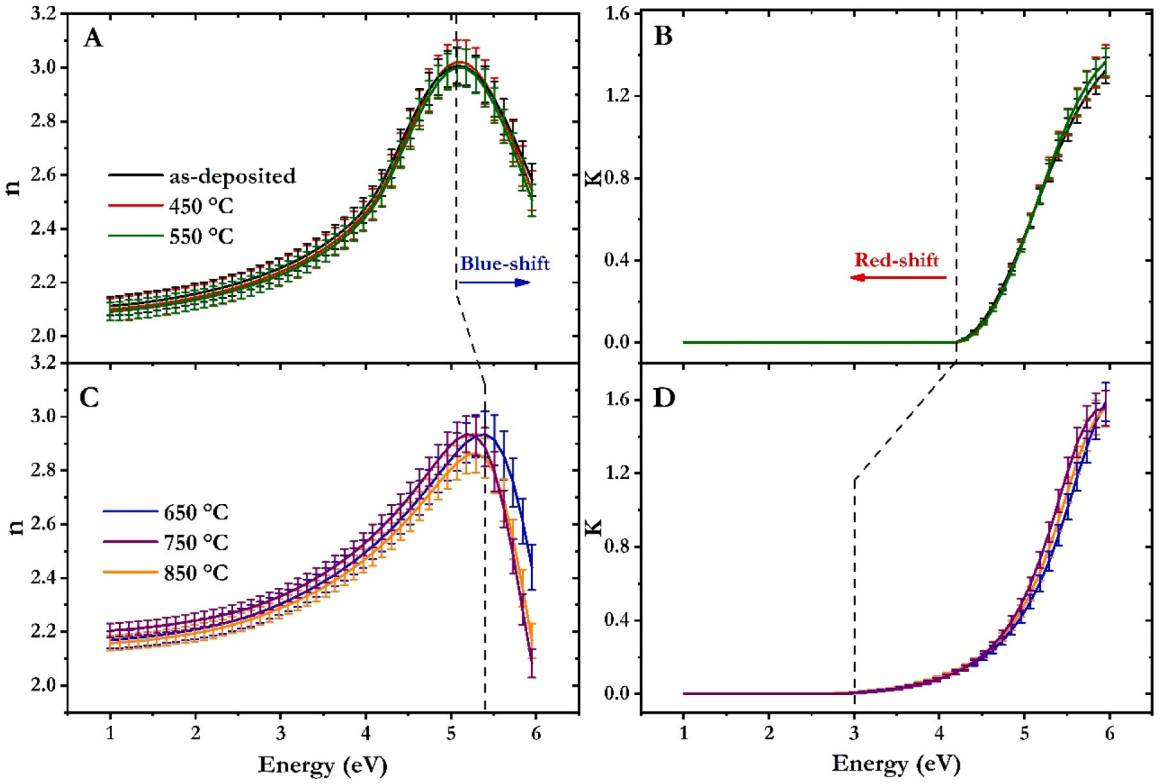

Fig. 7. (A)(C) Refractive index n, and (B)(D) extinction coefficient k of Ta_2O_5 thin films, grown at 3.28 W/cm² under 8 sccm, as a function of photon energy. Data is shown for both as-deposited and annealed samples at varying temperatures, with uncertainty represented by error bars.

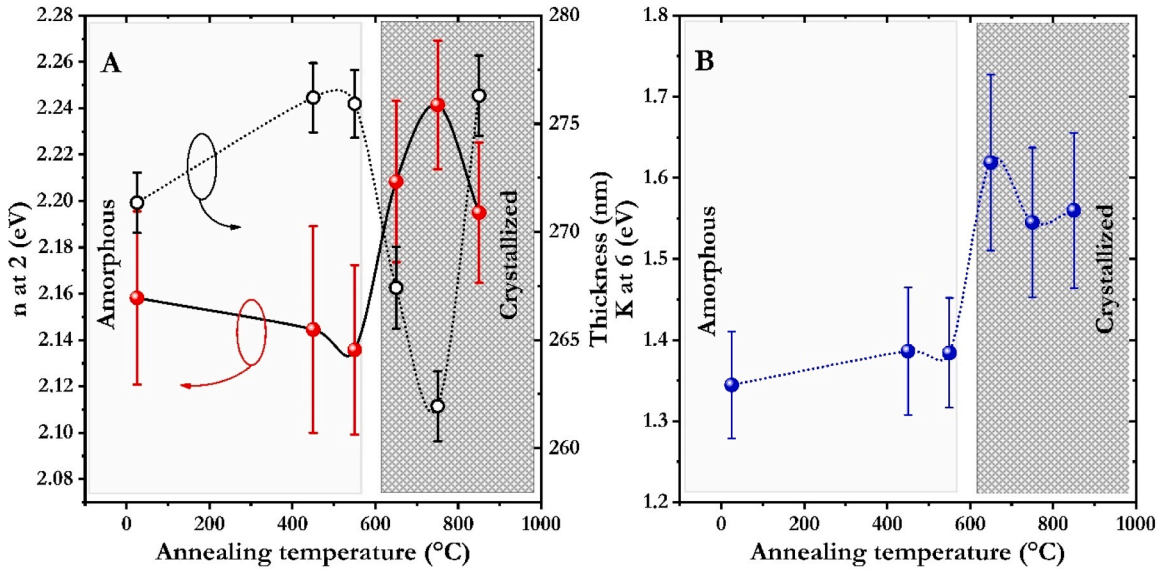

Fig. 8. (A) Evolution of the refractive index at 2 eV and film thickness, and (B) extinction coefficient at 6 eV for Ta_2O_5 films annealed between 450 °C and 850 °C. The colored regions indicate the amorphous and crystalline phases based on annealing temperature; with the lines serving as a guide to the eye.

Considering its potential effect, we determined α using the equation (2) through ρ_{RBS}, to establish a more accurate value and ensure the correlation between optical parameters and the material's chemical composition. Fig. 9(A) shows that the polarizability decreases from 1.51 ± 10^{-23} cm^{-3} to 1.47 ± 10^{-23} cm^{-3} upon annealing up to 650 °C, consistent with the observed densification and structural ordering, and comparable to reported TaO_y values [43]. Beyond this temperature, polarizability increases up to 1.52 ± 10^{-23} cm^{-3} at 850°C. This non-monotonic evolution reflects the density trend and is consistent with variations in $n_{2\,eV}$, $k_{6\,eV}$, and film thickness. The initial decrease in polarizability is attributed to the amorphous to crystalline transition, where denser atomic packing reduces the ability of electron clouds to distort, in accordance with the Clausius-Mossotti relation [67]. The subsequent increase at higher temperatures likely arises from defect formation or partial structural disorder, which enhances local polarizability. Since the dielectric response in our material is governed primarily by electronic polarization, these variations directly reflect changes in the electronic structure and local-field effects.

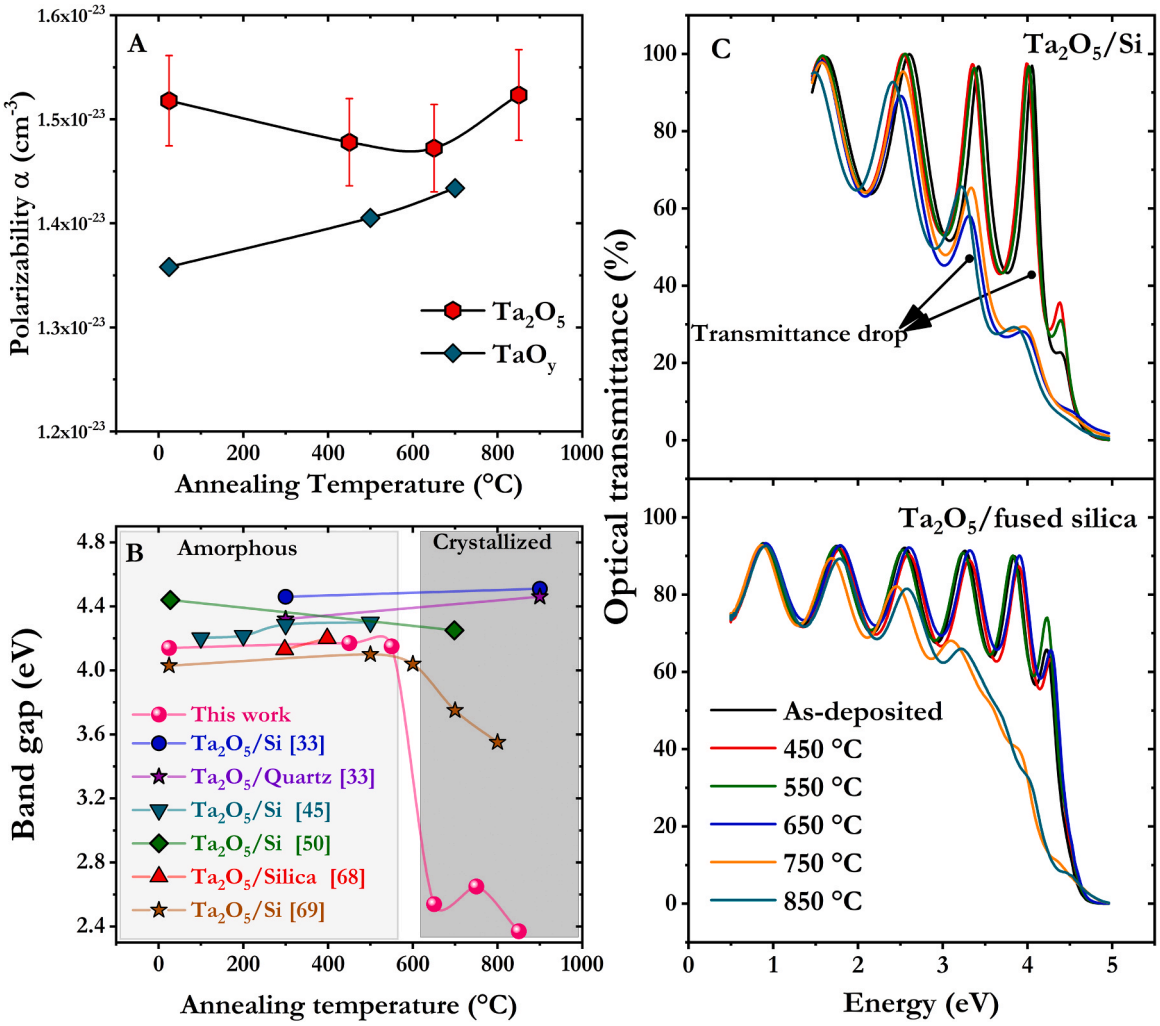

Fig. 9. (A) Optical molecular polarizabilities at 2 eV for Ta_2O_5/Si at different annealing temperatures, compared with literature values for TaO_y [43]. (B) Band gap energy of Ta_2O_5 as a function of annealing temperature from ellipsometry measurements, compared with literature data [33,45,50,68,69]. (C) Upper: Theoretical optical transmittance of the Ta_2O_5/Si heterostructure. Lower: Experimental optical transmittance of Ta_2O_5 on fused silica substrate, measured with TE polarization at 0°.

To explore the origin of the observed optical changes, we examined the evolution of the optical band gap using the TL model for both the as-deposited and annealed samples (Fig. 9(B)). A central aim of this study is to understand the changes in the electronic structure, as both the band gap and optical transmittance are highly sensitive to defects, which can significantly alter the nature and onset of optical transitions.

The presence of defects is further evidenced by the trend in the optical band gap (E_g) with annealing. The increase in E_g up to 550 °C is consistent with the compensation of oxygen vacancies in the amorphous phase, a behavior widely reported in the literature by Cheng et *al.* [68], D. Briand et *al.* [69], and T. Sertel et *al.* [45]. Beyond these annealing temperatures, the trend in E_g drastically reverses, decreasing to 2.54 eV at 650 °C (2.37 eV at 850 °C), suggesting the formation of oxygen vacancies. This behavior contrasts sharply with the findings of W. Ren et *al.* [33], where annealing treatment enhanced crystallinity and reduced oxygen vacancy concentration. In that study, E_g was observed to increase from 4.46 (300 °C) to 4.51 eV (900 °C), an effect attributed to the diffusion of Si into Ta_2O_5 films, forming SiO_2 and tantalum silicate at the interface. Such variation in structural quality is opposed to the optical trends observed in our study.

However, other theoretical studies show that introducing oxygen vacancies in Ta_2O_5 leads to the formation of defect states near the conduction band edge [36]. These states can participate in optical transitions, reinforcing the possible role of oxygen vacancies in the observed optical variations. The significant decrease in the band gap can be explained by the fact that in amorphous Ta_2O_5, the delocalized states and the presence of localized tail states near the band edges hinder electron transitions into conductive states [70,71]. This results in a wider band gap than that in its crystalline form. Crystalline phases introduce shallow defects or tail states near the band edges, such as oxygen vacancies, which contribute to the observed reduction in the optical band gap. This is confirmed by RBS and TEM measurements, which show a slight oxygen deficiency and migration towards the substrate interface in the annealed samples. Additionally, the formation of voids at 850 °C could contribute to the creation of localized states within the band gap [72]. In comparison with alternative hypotheses from the literature, such as the formation of SiO_2, crystallization, changes in the nature of the band gap, or Ta clustering, our findings clearly indicate that oxygen vacancies, by introducing mid-gap states, are responsible for sub-bandgap absorption. These oxygen vacancies (V_o), singly charged (V^+), and doubly charged (V^{2+}) act as active color centers by introducing defect states within the band gap of Ta_2O_5. Typically, V_o introduces a shallow donor level approximately 0.5–1.2 eV below the conduction band minimum (CBM), V^+ creates a mid-gap state around 1.5–2.0 eV below the CBM, and V^{2+} can result in deeper levels up to 2.5 eV below the CBM [73–75]. These states facilitate sub-bandgap photon

absorption, thereby reducing optical transparency. The corresponding increase in the extinction coefficient (k) near 3 eV observed in annealed, crystallized samples suggests a narrowing of the UV transparency window. Therefore, optical transmittance measurements are required to confirm this hypothesis.

To explore the optical impact of these changes, we combined theoretical and experimental approaches to measure transmittance. Since the silicon substrate is nontransparent, we performed theoretical calculations of optical transmittance by applying the TL model parameters obtained from fitting the samples optical reflectivity measured by URA using the TMM method. In parallel, we measured the optical transmittance of Ta_2O_5 grown on fused silica substrate due to its transparency in the visible range. As shown in Fig. 9(C), the as-deposited Ta_2O_5/Si and annealed films up to 550 °C exhibit high optical transmittance at lower energies, with distinct interference patterns, and remain relatively stable. Sharp transmittance drop was observed at 4.5 eV for annealing temperatures up to 550 °C, attributed to direct optical transitions within the Ta_2O_5 band gap.

However, a notable reduction in transmittance is observed above 3.5 eV for samples annealed above 650 °C, reflecting changes in the Ta_2O_5 film optical properties. This spectral redshift is associated with a contraction of the band gap to 2.54 eV at 650 °C and a concurrent rise in the extinction coefficient (k) at 3 eV. Such optical behavior suggests the onset of sub-bandgap absorption, rather than inter-band optical transitions from O-*p* to Ta-*d* orbitals. In fact, high temperature annealing induces defects that generate mid-gap states, likely due to oxygen vacancies, forming a band-tail extending to 2.54 eV at $T_A = 650$ °C (2.37 eV at T_A=850°C). Concurrently, the increase in the extinction coefficient (k) reflects earlier absorption relative to the standard 4 eV onset observed in the amorphous samples. The convergence of band tailing, the rise in the extinction coefficient (k), and the transmittance drop offer strong evidence for the role of defects on optical properties. The theoretical transmittance of Ta_2O_5/Si closely matches the experimental transmittance of Ta_2O_5/fused silica, although with reduced interference effects, probably due to changes in the film structure. Comparing both results, the transmittance of Ta_2O_5/fused silica shows no significant drop until annealing temperatures exceed 750 °C. This delayed decrease in transmittance may be attributed to differences in thermal behavior, arising from the distinct properties of the Si and fused silica substrates.

To understand the role of oxygen vacancies, one must consider that while both samples annealed at 450 °C and 650 °C maintain a Ta/O ratio of 0.415, only the crystalline film annealed at 650 °C reveals an enhancement in sub-bandgap absorption. This suggest that crystallization may render the optical transition allowed. Furthermore, the persistence of these optical transitions at 850 °C, despite a lower density of oxygen vacancies (as indicated by a Ta/O ratio of 0.39), implies that ordered regions retains the conditions for these transitions to remain active.

Since TEM analysis reveals no signs of metallic inclusions and clustering at higher T_A, the observed band gap narrowing is unlikely to result from compositional changes. This contrasts with the case reported by M. Cevro *et al.* [26], where metallic Ta clusters significantly reduced the band gap (E_g) to 0 eV.

Additionally, theoretical work by S. Sathasivam [76] suggests that the reduction in the band gap (E_g) of Ta_2O_5 may result from a transition from an indirect to a direct band gap upon crystallization. A similar trend was observed in Nb_2O_5, a closely related material, during the annealing process [21]. While both crystallization and phase transitions induced by thermal annealing can significantly alter the electronic structure of Ta_2O_5, these factors alone cannot explain the drastic band gap reduction from 4 to 2 eV observed in our samples.

To better understand the mechanism driving the changes in refractive index and extinction coefficient, and to compare with existing literature, we refer to a prior study on Ta_2O_5 synthesized through plasma-enhanced chemical vapor deposition (PECVD) using $Ta(OC_2H_5)_5$ precursors [15]. As reported in Table 2, the presence of Carbon in the Ta_2O_5/Si system has an impact on the refractive index. Once carbon removal initiates at 400 °C, the resulting decrease in film density leads to a decrease in n by roughly 4 % from 2.13 for as-deposited to 2.05 for films annealed at 600 °C. Upon further annealing, crystallization at 800 °C recovers n by increasing film density, generating optical scattering at grain boundaries. Despite this recovery, the reported values remain lower than those achieved in our study (2.13–2.24). Another work on the same system deposited by low-pressure chemical vapor deposition (CVD) with the same precursor showed an increase in n from 2.15 to 2.24 at 800 °C, which closely aligns with our results. The incomplete removal of carbon shows that it acts as a stabilizer, contributing alongside densification to the observed index enhancement [23]. Unlike carbon-assisted methods, our sputtered films achieve higher indices, through densification, in agreement with similar sputtering studies [35, 42,77]. As densification was not quantified in those studies, our study demonstrates its correlation with crystallization and optical changes. Based on the refractive index, we derived the Ta_2O_5's density through the Lorentz-Lorentz law. Despite the underestimated density due to the use of approximate polarizability values, the obtained values follow the same behavior as those from RBS measurements. To address this, we refined the accuracy of Ta_2O_5's polarizability by aligning it with RBS-measured densities and propose a revised set of reference values at different annealing temperatures.

The cationic ratio Ta/O plays a crucial role in tuning the refractive index and the extinction coefficient. The Ta_2O_5/Si system grown by pulsed laser deposition (PLD) shows a high sensitivity of the Ta/O to the oxygen pressure [24]. A substantial increase in the ratio to 0.65 is observed under low pressure, while higher oxygen environment reduces it to 0.40. A similar trend was observed in our sputtered films, with a drop in Ta/O from 0.44 to 0.415. Low-oxygen films show higher n$\sim$ 2.72–3.1 but suffer from high optical losses, whereas oxygen-rich films achieve a desirable balance between good n$\sim$ 2.25–2.30 and low absorption ($<10^{-4}$) (See Table 2).

The band gap changes in response to thermal process, impacted by structural evolution and variation in the film's microstructure. The Ta_2O_5/quartz system shows a decrease in the band gap (from 4.39 to 4.25 eV), accompanied by a decline in optical transmission (77–73 %) and a restriction of the optical transparency window, reflecting the effect of packing densification and crystallinity [50]. Other studies on quartz report a reduction in E_g attributed to weak Si diffusion, while transparency remains unaffected since crystallization is delayed until 900 °C [33] (See Table 2).

One of the most remarkable outcomes of our study is the significant 50 % reduction in band gap upon crystallization, relative to previously reported values (See Fig. 9(B)). While such variations are often attributed to changes in the electronic structure, the pronounced reduction implies an additional effect, the formation of defect states within the band gap. These are mostly due to oxygen vacancies, a conclusion reinforced by RBS measurements revealing oxygen deficiency in annealed samples (Ta/O=0.415). At higher annealing temperatures, further structural changes such as void formation are observed, potentially leading to additional mid-gap states. We also addressed a limitation in characterizing the optical transparency of Ta_2O_5 grown on an opaque substrate, such as silicon. By applying the parameters obtained from reflectivity fitting within the TMM framework, we quantified the theoretical transmittance without requiring transparent substrates. The correlation between the transmittance trends, bandgap reduction, and increased extinction coefficient supports the presence of trap states acting as absorption centers.

We investigated the optical performance of our films by following changes in the optical transparency window size (E_{size}= $E_{1.55\ eV}$-$E_{interband}$) relative to the refractive index. Here, the $E_{1.55\ eV}$ was fixed at the visible-NIR boundary due to insufficient of available data beyond this energy, and $E_{interband}$ reflects the transmittances drop at the UV–visible boundary. As shown in Fig. 10, despite being grown on opaque Si

Table 2
Comparative table of refractive index n, extinction coefficient k, cationic ratio Ta/O, band gap energy E_g, transmittance T, and optical transparency window.

Methods	Substrate	Condition		n	k	Ta/O	Eg (eV)	T (%)	Transparency Window E_{size} (eV)
		T(°C)	Pressure						
PECVD [15]		AD	-	2,13	$< 10^{-4}$			-	
		400		2,11					
		600		2,05					
		800		2,075	0,02				
LPCVD [23]		AD	-	2,156			-		
		800 (O2)		2,243					
RF-sputtering [77]	Si	AD	10^{-6} (Torr)	2,13	-		4,65		-
		200		2,16			4,73		
RF-sputtering [35]		AD	3,3 (Pa)	2,10			-		
		600							
PLD [24]		AD	0,14 (Pa)	3,10	0,7	0,6	0,5		-
			2,67 (Pa)	2,25	$< 10^{-4}$	0,65	4		
		400	0,14 (Pa)	2,72	0,45	0,43	1		
			2,67 (Pa)	2,30	$< 10^{-4}$	0,4	4		
dc-sputtering [50]	Quartz	AD	2×10^{-6} (mbar)	2,02	-		4,44	70	1,55*–3,87
		500		2,15			4,39	77	1,55*–3,64
		700		2,25			4,25	73	1,55*–3,10
PIAD [25]		AD	-	2,02	$< 10^{-4}$			-	
		375		2,16					
IAD [46]	Silica	250	25 (Sccm)	2,17	-		4,17	80	1,55*–4,42
			30 (Sccm)	2,166			4,20		
			35 (Sccm)	2,165			4,14		
EBE [33]	Si	300	-	-			4,46	-	
		900					4,51		
	Quartz	300					4,32		1,55*–4,42
		900					4,46		

* Set at 1.55 eV to align available data and ensure uniform comparison.

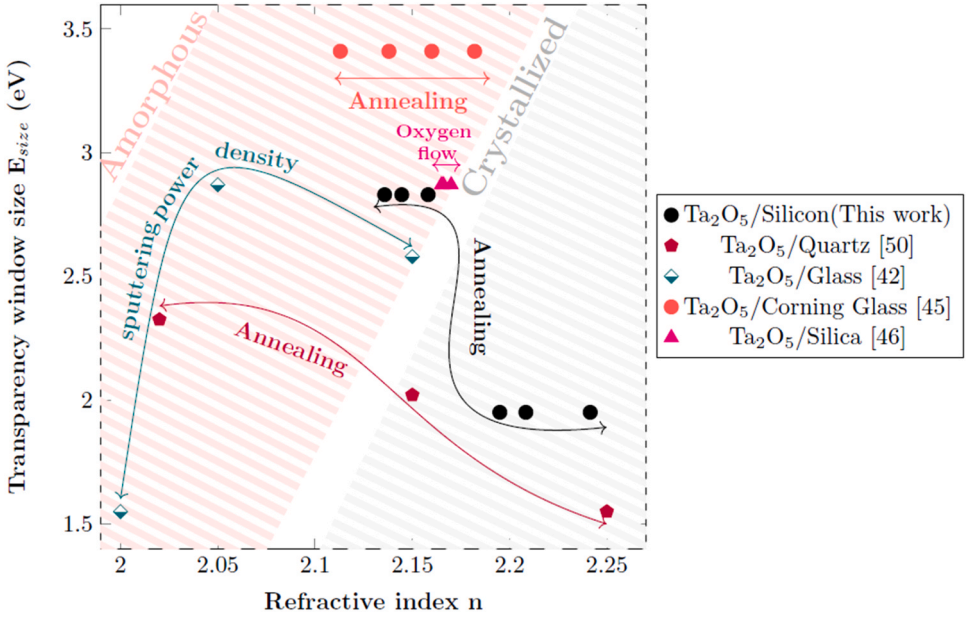

Fig. 10. Optical performance of high refractive-index transparent Ta_2O_5: Transparency window size E_{size} as a function of refractive index n. The grey dashed region represents crystallized films, while pink region corresponds to amorphous films. Arrows reflect the processing steps (growth conditions and annealing process).

substrate, our results are in strong agreement with studies on transparent substrates, confirming the reliability of our theoretical approach. Upon crystallization, E_{size} decreased by 33 %, which can be attributed to the formation of defect states within the band gap, such as the presence of oxygen vacancies. Meanwhile, the increase in n reflects the densification of Ta_2O_5 during crystallization. According to the desired functionality, the refractive index of Ta_2O_5 can be enhanced at the expense of the transparency window size through crystallization.

4. Conclusion

Ta_2O_5 thin films were deposited by radio-frequency sputtering from a high-purity Ta_2O_5 target onto silicon substrates. Optimal growth conditions, achieved at a sputtering power density of at least 3.29 W/cm^2 and an oxygen flow rate of 8 sccm, resulted in near-stoichiometric Ta_2O_5 with a Ta/O cationic ratio of 0.38 and film density around 7.50 g.cm^{-3}, close to the bulk value, as confirmed by RBS. Under these conditions, amorphous Ta_2O_5 films with a refractive index $n_{2\,eV}$= 2.14 and a negligible extinction coefficient ($k < 10^{-4}$) over UV–visible-IR

spectral range (1.55–4 eV) were obtained.

In the second phase of the study, the deposited films underwent Rapid Thermal Annealing (RTA) at temperatures ranging from 450 °C to 850 °C, in 100 °C increments. X-ray diffraction (XRD) measurements indicated the onset of crystallization at 650 °C, with the orthorhombic phase becoming dominant at higher temperatures. Transmission Electron Microscopy (TEM) further confirmed this progression, revealing an amorphous structure at 450 °C, a mixed amorphous/crystalline phase at 650 °C, and the formation of void cavities at 850 °C, suggesting degradation of the crystalline matrix at elevated temperatures.

Following crystallization, the refractive index reached a maximum of 2.24 at 750 °C, before declining to 2.18 at 850 °C. This trend is due to densification occurring between 650 °C and 750 °C from 7.62 to 7.85 g.cm^{-3}, followed by density degradation to 7.55 g.cm^{-3} at 850 °C. In parallel, the extinction coefficient onset redshifts from 4 to 3 eV, accompanied by a significant reduction of the band gap E_g from 4 to 2.54 eV at 650 °C (2.37 eV at 850 °C). This restriction results from the creation of mid-gap states, likely due to oxygen vacancies, which lead to sub-bandgap absorption and limit the size of transparency window to 1.83 eV.

Amorphous Ta_2O_5 exhibits the optimal balance of optical properties compared to its crystalline counterpart, with a refractive index $n_{2\,eV}$= 2.15, negligible extinction coefficient, and an extended transparency window in the 1.55–4.5 eV range (275–826 nm). These characteristics make it particularly suitable for advanced optical applications, supporting its use in optical coatings for filters, waveguides, and metasurface materials.

CRediT authorship contribution statement

Christophe Labbé: Validation, Supervision, Investigation, Conceptualization. **Xavier Portier:** Writing – original draft, Visualization, Validation, Methodology, Investigation, Formal analysis, Data curation. **Jeremie Gonçalves:** Software, Investigation, Formal analysis. **Julien Cardin:** Writing – original draft, Visualization, Validation, Software, Methodology, Investigation, Formal analysis, Data curation, Conceptualization. **Aïmane Cheikh:** Writing – review & editing, Writing – original draft, Visualization, Methodology, Investigation, Formal analysis, Data curation, Conceptualization. **Wojciech Jadwisienczak:** Investigation. **David Ingram:** Investigation. **Olivier Debieu:** Investigation, Data curation, Conceptualization. **Sylvain Duprey:** Investigation. **Philippe Marie:** Visualization, Validation, Investigation, Data curation. **Cedric Frilay:** Investigation.

Declaration of Competing Interest

The authors decleare that this research received no specific funding from any institute or organization.

Appendix A. Supporting information

Supplementary data associated with this article can be found in the online version at doi:10.1016/j.jallcom.2025.183273.

References

[1] W.C. Herrmann Jr., E-beam deposition characteristics of reactively evaporated Ta2O5 for optical interference coatings, J. Vac. Sci. Technol. 18 (1981) 1303–1305, https://doi.org/10.1116/1.570921.
[2] F. Rubio, J. Denis, J.M. Albella, J.M. Martinez-Duart, Sputtered Ta2O5 antireflection coatings for silicon solar cells, Thin Solid Films 90 (1982) 405–408, https://doi.org/10.1016/0040-6090(82)90545-4.
[3] C. Christensen, R. de Reus, S. Bouwstra, Tantalum oxide thin films as protective coatings for sensors, J. Micromech. Microeng. 9 (1999) 113, https://doi.org/10.1088/0960-1317/9/2/003.
[4] Y.-K. Tu, C.-C. Lin, W.-S. Wang, S.-L. Huang, Characterization of reactively r.f.-sputtered tantalum oxide films, Thin Solid Films 162 (1988) 325–331, https://doi.org/10.1016/0040-6090(88)90221-0.
[5] K. Schmitt, K. Oehse, G. Sulz, C. Hoffmann, Evanescent field sensors based on tantalum pentoxide waveguides - a review, Sensors 8 (2008) 711–738, https://doi.org/10.3390/s8020711.
[6] C. Chaneliere, J.L. Autran, R.A.B. Devine, B. Balland, Tantalum pentoxide (Ta2O5) thin films for advanced dielectric applications, Mater. Sci. Eng. R. Rep. 22 (1998) 269–322, https://doi.org/10.1016/S0927-796X(97)00023-5.
[7] C.H. Kao, P.L. Lai, H.Y. Wang, The comparison between Ta2O5 and Ti-doped Ta2O5 dielectrics, Surf. Coat. Technol. 231 (2013) 512–516, https://doi.org/10.1016/j.surfcoat.2012.04.045.
[8] R. Fan, Y.-Y. Lin, L. Chang, A. Boes, J. Bowers, J.-W. Liu, C.-H. Lin, T.-K. Wang, J. Qiao, H.-C. Kuo, G.-R. Lin, M.-H. Shih, Y.-J. Hung, Y.-J. Chiu, C.-K. Lee, Higher order mode supercontinuum generation in tantalum pentoxide (Ta2O5) channel waveguide, Sci. Rep. 11 (2021) 7978, https://doi.org/10.1038/s41598-021-86922-8.
[9] J.H. Sierra, R.C. Rangel, R.E. Samad, N.D. Vieira, M.I. Alayo, D.O. Carvalho, Low-loss pedestal Ta_2O_5 nonlinear optical waveguides, Opt. Express 27 (2019) 37516–37521, https://doi.org/10.1364/OE.27.037516.
[10] J.H. Sierra, D.O. Carvalho, L.R.P. Kassab, C.D. da Silva Bordon, R.E. Samad, N. U. Wetter, M.I. Alayo, Pedestal waveguides based on GeO2-Bi2O3, GeO2-PbO, Ta2O5 and SiOxNy cores as platforms for optical amplifiers and nonlinear optics applications: review of recent advances, J. Lumin 236 (2021) 118113, https://doi.org/10.1016/j.jlumin.2021.118113.
[11] Y. Sekido, Characteristics of ta2O5 thin film prepared by electron beam heating method, Electron. Commun. Jpn. Part II Electron. 77 (1994) 54–61, https://doi.org/10.1002/ecjb.4420770607.
[12] I. Porqueras, J. Marti, E. Bertran, Optical and electrical characterisation of Ta2O5 thin films for ionic conduction applications, Thin Solid Films 343–344 (1999) 449–452, https://doi.org/10.1016/S0040-6090(99)00121-2.
[13] E.B. Franke, C.L. Trimble, M. Schubert, J.A. Woollam, J.S. Hale, All-solid-state electrochromic reflectance device for emittance modulation in the far-infrared spectral region, Appl. Phys. Lett. 77 (2000) 930–932, https://doi.org/10.1063/1.1288810.
[14] X. He, J. Wu, X. Li, X. Gao, L. Wu, L. Zhao, X. Gan, F. Zhuge, Characterization of high quality tantalum pentoxide film synthesized by oxygen plasma enhanced pulsed laser deposition, Thin Solid Films 518 (2009) 94–98, https://doi.org/10.1016/j.tsf.2009.06.041.
[15] J.-P. Masse, H. Szymanowski, O. Zabeida, A. Amassian, J.E. Klemberg-Sapieha, L. Martinu, Stability and effect of annealing on the optical properties of plasma-deposited Ta2O5 and Nb2O5 films, Thin Solid Films 515 (2006) 1674–1682, https://doi.org/10.1016/j.tsf.2006.05.047.
[16] K.D. Pollard, R.J. Puddephatt, Chemical vapor deposition of tantalum oxide from Tetraethoxo(β-diketonato)tantalum(V) complexes, Chem. Mater. 11 (1999) 1069–1074, https://doi.org/10.1021/cm981047a.
[17] H.J. Quah, F.H. Ahmad, W.F. Lim, Z. Hassan, Growth and characterization of ternary HfxTayOz films via Nitrogen-Infused wet oxidation, ACS Omega 5 (2020) 26347–26356, https://doi.org/10.1021/acsomega.0c02120.
[18] C. Zhang, L. Chen, Z. Lin, J. Song, D. Wang, M. Li, O. Koksal, Z. Wang, G. Spektor, D. Carlson, H.J. Lezec, W. Zhu, S. Papp, A. Agrawal, Tantalum pentoxide: a new material platform for high-performance dielectric metasurface optics in the ultraviolet and visible region, Light Sci. Appl. 13 (2024) 23, https://doi.org/10.1038/s41377-023-01330-z.
[19] Mc.D. Robinson, Silicon epitaxy, in: R.A. Levy (Ed.), Microelectron. Mater. Process, Springer Netherlands, Dordrecht, 1989, pp. 25–78, https://doi.org/10.1007/978-94-009-0917-5_2.
[20] J.T. Clemens, Silicon microelectronics technology, Bell Labs Tech. J. 2 (2002) 76–102, https://doi.org/10.1002/bltj.2084.
[21] B. Horcholle, C. Labbé, X. Portier, P. Marie, C. Frilay, W. Yuan, W. Jadwisienczak, D. Ingram, C. Grygiel, J. Cardin, Growth and study of Tb3+ doped Nb2O5 thin films by radiofrequency magnetron sputtering: photoluminescence properties, Appl. Surf. Sci. 597 (2022) 153711, https://doi.org/10.1016/j.apsusc.2022.153711.
[22] S. Larouche, H. Szymanowski, J.E. Klemberg-Sapieha, L. Martinu, S.C. Gujrathi, Microstructure of plasma-deposited SiO2/TiO2 optical films, J. Vac. Sci. Technol. A 22 (2004) 1200–1207, https://doi.org/10.1116/1.1763912.
[23] C. Chaneliere, S. Four, J.L. Autran, R.A.B. Devine, N.P. Sandler, Properties of amorphous and crystalline Ta2O5 thin films deposited on si from a Ta(OC2H5)5 precursor, J. Appl. Phys. 83 (1998) 4823–4829, https://doi.org/10.1063/1.367277.
[24] S. Boughaba, M.U. Islam, G.I. Sproule, M.J. Graham, Characterization of tantalum oxide films grown by pulsed laser deposition, Surf. Coat. Technol. 120–121 (1999) 757–764, https://doi.org/10.1016/S0257-8972(99)00371-0.
[25] H. Szymanowski, O. Zabeida, J.E. Klemberg-Sapieha, L. Martinu, Optical properties and microstructure of plasma deposited Ta2O5 and Nb2O5 films, J. Vac. Sci. Technol. A 23 (2005) 241–247, https://doi.org/10.1116/1.1851544.
[26] M. Cevro, G. Carter, Ion-beam and dual-ion-beam sputter deposition of tantalum oxide films, Opt. Eng. 34 (1995) 596–606, https://doi.org/10.1117/12.188616.
[27] S.-O. Kim, H.J. Kim, The effects of substrate and annealing ambient on the electrical properties of Ta2O5 thin films prepared by plasma enhanced chemical vapor deposition, Thin Solid Films 253 (1994) 435–439, https://doi.org/10.1016/0040-6090(94)90362-X.
[28] I. Perez, J.L.E. Carrejo, V. Sosa, F.G. Perera, J.R.F. Mancillas, J.T.E. Galindo, C.I. R. Rodríguez, Evidence for structural transition in crystalline tantalum pentoxide films grown by RF magnetron sputtering, J. Alloy. Compd. 712 (2017) 303–310, https://doi.org/10.1016/j.jallcom.2017.04.073.
[29] P.C. Joshi, M.W. Cole, Influence of postdeposition annealing on the enhanced structural and electrical properties of amorphous and crystalline Ta2O5 thin films

for dynamic random access memory applications, J. Appl. Phys. 86 (1999) 871–880, https://doi.org/10.1063/1.370817.
[30] Z.-W. Fu, F. Huang, Y.-Q. Chu, Y. Zhang, Q.-Z. Qin, Characterization of amorphous Ta2 o 5 film as a novel anode material, J. Electrochem. Soc. 150 (2003) A776, https://doi.org/10.1149/1.1573194.
[31] M.S. Farhan, E. Zalnezhad, A.R. Bushroa, Properties of Ta2O5 thin films prepared by ion-assisted deposition, Mater. Res. Bull. 48 (2013) 4206–4209, https://doi.org/10.1016/j.materresbull.2013.06.068.
[32] W.-J. Liu, X.-J. Guo, C.-H. Chien, The study of optical and microstructural evolution of Ta2O5 and SiO2 thin films by plasma ion assisted deposition method, Surf. Coat. Technol. 196 (2005) 69–75, https://doi.org/10.1016/j.surfcoat.2004.08.098.
[33] W. Ren, G.-D. Yang, A.-L. Feng, R.-X. Miao, J.-B. Xia, Y.-G. Wang, Annealing effects on the optical and electrochemical properties of tantalum pentoxide films, J. Adv. Ceram. 10 (2021) 704–713, https://doi.org/10.1007/s40145-021-0465-2.
[34] D. Gu, J. Li, S.K. Dey, H. De Waard, S. Marcus, Nanochemistry, nanostructure, and electrical properties of Ta2O5 film deposited by atomic layer deposition and plasma-enhanced atomic layer deposition, J. Vac. Sci. Technol. B Microelectron. Nanometer Struct. Process. Meas. Phenom. 24 (2006) 2230–2235, https://doi.org/10.1116/1.2335432.
[35] T. Dimitrova, K. Arshak, E. Atanassova, Crystallization effects in oxygen annealed Ta2O5 thin films on si, Thin Solid Films 381 (2001) 31–38, https://doi.org/10.1016/S0040-6090(00)01569-8.
[36] M.S. Islam, J. Lee, S. Ganguli, A.K. Roy, Effect of oxygen vacancy and si doping on the electrical properties of Ta2O5 in memristor characteristics, Sci. Rep. 13 (2023) 16656, https://doi.org/10.1038/s41598-023-43888-z.
[37] J. Wasyluk, T.S. Perova, F. Meyer, Raman and Fourier transform infrared study of substitutional carbon incorporation in rapid thermal chemical vapor deposited Si1−x−yGexCy on (1 0 0) si, J. Appl. Phys. 107 (2010) 023518, https://doi.org/10.1063/1.3284937.
[38] M. Abbasi–Nahr, S.E. Mirsalehi, Additive friction stir deposition of AA5083/MoS2-diamond hybrid nanocomposites: investigating their metallurgical, mechanical, tribological, and electrochemical characteristics, and process-structure-property relationships, J. Alloy. Compd. 1013 (2025) 178553, https://doi.org/10.1016/j.jallcom.2025.178553.
[39] M. Abbasi Nahr, S.E. Mirsalehi, A. Papi, Additive manufacturing of AA2024/Al2O3 nanocomposites via friction surfacing: investigating metallurgical, mechanical, and tribological properties, J. Mater. Res. Technol. 36 (2025) 8609–8631, https://doi.org/10.1016/j.jmrt.2025.05.124.
[40] M. Abbasi-Nahr, S.E. Mirsalehi, S.S. Mirhosseini, Additive manufacturing of AA5083/TiN-Diamond hybrid nanocomposite parts via additive friction stir deposition: metallurgical structure, mechanical, tribological, and electrochemical properties, J. Mater. Res. Technol. 30 (2024) 8187–8208, https://doi.org/10.1016/j.jmrt.2024.05.158.
[41] H. Razmjoo, S.E. Mirsalehi, M. Abbasi-Nahr, M. Navidi-Helan, Microstructure, corrosion, and tribological performance of multilayered cylindrical AA5083 parts fabricated by modified friction stir deposition – additive manufacturing, Mater. Charact. 221 (2025) 114777, https://doi.org/10.1016/j.matchar.2025.114777.
[42] X. Chen, R. Bai, M. Huang, Optical properties of amorphous Ta2O5 thin films deposited by RF magnetron sputtering, Opt. Mater. 97 (2019) 109404, https://doi.org/10.1016/j.optmat.2019.109404.
[43] E. Cetinörgü-Goldenberg, J.-E. Klemberg-Sapieha, L. Martinu, Effect of postdeposition annealing on the structure, composition, and the mechanical and optical characteristics of niobium and tantalum oxide films, Appl. Opt. 51 (2012) 6498–6507, https://doi.org/10.1364/AO.51.006498.
[44] T. Plirdpring, M. Horprathum, C. Chananonnawathorn, P. Eiamchai, A. Harnwunggmoung, T. Boonpichayapha, P. Lorwongtragool, A. Charoenphakdee, Effect of annealing temperature on structure and optical properties of Ta2O5 thin films prepared by DC magnetron sputtering, Adv. Mater. Res. 770 (2013) 149–152, https://doi.org/10.4028/www.scientific.net/AMR.770.149.
[45] T. Sertel, N.A. Sonmez, S.S. Cetin, S. Ozcelik, Influences of annealing temperature on anti-reflective performance of amorphous Ta2O5 thin films, Ceram. Int. 45 (2019) 11–18, https://doi.org/10.1016/j.ceramint.2018.09.237.
[46] L. Wang, W. Zhang, R. Hong, K. Wang, M. Wang, Q. Wang, K. Yi, J. Shao, Reduction of absorption of Ta2O5 monolayers through the suppression of structural defects by employing an appropriate ionic oxygen concentration, Sci. Rep. 15 (2025) 4124, https://doi.org/10.1038/s41598-025-86151-3.
[47] P.-H. Chang, H.-Y. Liu, Structures of tantalum pentoxide thin films formed by reactive sputtering of ta metal, Thin Solid Films 258 (1995) 56–63, https://doi.org/10.1016/0040-6090(94)06402-4.
[48] A. Reisman, F. Holtzberg, M. Berkenblit, M. Berry, Reactions of the group VB pentoxides with alkali oxides and carbonates. Iii. thermal and X-Ray phase diagrams of the system K2O or K2CO3 with Ta2O5, J. Am. Chem. Soc. 78 (1956) 4514–4520, https://doi.org/10.1021/ja01599a003.
[49] M.-K. Kim, W.-H. Kim, T. Lee, H. Kim, Growth characteristics and electrical properties of Ta2O5 grown by thermal and O3-based atomic layer deposition on TiN substrates for metal–insulator–metal capacitor applications, Thin Solid Films 542 (2013) 71–75, https://doi.org/10.1016/j.tsf.2013.06.050.
[50] S.V.J. Chandra, S. Uthanna, G.M. Rao, Effect of substrate temperature on the structural, optical and electrical properties of dc magnetron sputtered tantalum oxide films, Appl. Surf. Sci. 254 (2008) 1953–1960, https://doi.org/10.1016/j.apsusc.2007.08.005.
[51] K.K. Sahoo, D. Pradhan, A. Gartia, S.P. Ghosh, J.P. Kar, Suppression of oxide and interface charge density in radio frequency sputtered Ta2O5 thin films, Phys. Status Solidi A 221 (2024) 2300292, https://doi.org/10.1002/pssa.202300292.
[52] J.M. Purswani, A.P. Pons, J.T. Glass, R.D. Evans, J.D. Cogdell, Effects of annealing on the mechanical and electrical properties of DC sputtered tantalum pentoxide (Ta2O5) thin films, MRS Online Proc. Libr 811 (2003) 197–202, https://doi.org/10.1557/PROC-811-D3.8.
[53] S. Kimura, Y. Nishioka, A. Shintani, K. Mukai, Leakage-Current increase in amorphous Ta2 o 5 films due to pinhole growth during annealing below 600°C, J. Electrochem. Soc. 130 (1983) 2414, https://doi.org/10.1149/1.2119599.
[54] J. Harvey, H. Wilman, The crystallisation of thin amorphous tantalum oxide films heated in air or vacuo, and the structure of the crystalline oxide, Acta Crystallogr 14 (1961) 1278–1281, https://doi.org/10.1107/S0365110X61003703.
[55] G. Sethi, B. Bontempo, E. Furman, M.W. Horn, M.T. Lanagan, S.S.N. Bharadwaja, J. Li, Impedance analysis of amorphous and polycrystalline tantalum oxide sputtered films, J. Mater. Res. 26 (2011) 745–753, https://doi.org/10.1557/jmr.2010.77.
[56] A. Krishnaprasanth, M. Seetha, Solvent free synthesis of Ta2O5 nanoparticles and their photocatalytic properties, AIP Adv. 8 (2018) 055017, https://doi.org/10.1063/1.5019423.
[57] T.J. Bright, J.I. Watjen, Z.M. Zhang, C. Muratore, A.A. Voevodin, D.I. Koukis, D. B. Tanner, D.J. Arenas, Infrared optical properties of amorphous and nanocrystalline Ta2O5 thin films, J. Appl. Phys. 114 (2013) 083515, https://doi.org/10.1063/1.4819325.
[58] K. Lehovec, Lattice structure of β-Ta2O5, J. Common Met. 7 (1964) 397–410, https://doi.org/10.1016/0022-5088(64)90036-0.
[59] T. Jutarosaga, J.S. Jeoung, S. Seraphin, Infrared spectroscopy of Si–O bonding in low-dose low-energy separation by implanted oxygen materials, Thin Solid Films 476 (2005) 303–311, https://doi.org/10.1016/j.tsf.2004.10.006.
[60] E.S. Andrés, M. Toledano-Luque, A. del Prado, M.A. Navacerrada, I. Mártil, G. González-Díaz, W. Bohne, J. Röhrich, E. Strub, Physical properties of high pressure reactively sputtered TiO2, J. Vac. Sci. Technol. A 23 (2005) 1523–1530, https://doi.org/10.1116/1.2056554.
[61] O. Debieu, D. Bréard, A. Podhorodecki, G. Zatryb, J. Misiewicz, C. Labbé, J. Cardin, F. Gourbilleau, Effect of annealing and nd concentration on the photoluminescence of Nd3+ ions coupled with silicon nanoparticles, J. Appl. Phys. 108 (2010) 113114, https://doi.org/10.1063/1.3510521.
[62] J. Cardin, D. Leduc, Determination of refractive index, thickness, and the optical losses of thin films from prism-film coupling measurements, Appl. Opt. 47 (2008) 894–900, https://doi.org/10.1364/AO.47.000894.
[63] L.V.R. Marcos, J.I. Larruquert, J.A. Méndez, J.A. Aznárez, Self-consistent optical constants of SiO_2 and Ta_2O_5 films, Opt. Mater. Express 6 (2016) 3622–3637, https://doi.org/10.1364/OME.6.003622.
[64] Y. Cheng, X. Huang, Z. Du, J. Xiao, Effect of sputtering power on the structure and optical band gap of SiC thin films, Opt. Mater. 73 (2017) 723–728, https://doi.org/10.1016/j.optmat.2017.09.031.
[65] R. Shakoury, S. Rezaee, F. Mwema, C. Luna, K. Ghosh, S. Jurečka, Ş. Ţălu, A. Arman, A. Grayeli Korpi, Multifractal and optical bandgap characterization of Ta2O5 thin films deposited by electron gun method, Opt. Quantum Electron 52 (2020) 95, https://doi.org/10.1007/s11082-019-2173-5.
[66] N. Sangwaranatee, M. Horprathum, J. Kaewkhao, Effect of O2 flow rate on structural and optical properties of tantalum oxide thin films prepared by DC reactive magnetron sputtering, Adv. Mater. Res. 979 (2014) 448–451, https://doi.org/10.4028/www.scientific.net/AMR.979.448.
[67] P. Beck, P. Brommer, J. Roth, H.-R. Trebin, Influence of polarizability on metal oxide properties studied by molecular dynamics simulations, J. Phys. Condens. Matter 24 (2012) 485401, https://doi.org/10.1088/0953-8984/24/48/485401.
[68] C. Xu, S. Yang, J.-F. Wang, J.-N. Niu, H. Ma, Y.-H. Qiang, J.-T. Liu, D.-W. Li, C.-X. Tao, Effect of oxygen vacancy on the band gap and nanosecond Laser-Induced damage threshold of Ta2O5 films, Chin. Phys. Lett. 29 (2012) 084207, https://doi.org/10.1088/0256-307X/29/8/084207.
[69] D. Briand, G. Mondin, S. Jenny, P.D. van der Wal, S. Jeanneret, N.F. de Rooij, O. Banakh, H. Keppner, Metallo-organic low-pressure chemical vapor deposition of Ta2O5 using TaC12H30O5N as precursor for batch fabrication of microsystems, Thin Solid Films 493 (2005) 6–12, https://doi.org/10.1016/j.tsf.2005.03.021.
[70] B. Xiao, T. Gu, T. Tada, S. Watanabe, Conduction paths in Cu/amorphous-Ta2O5/Pt atomic switch: First-principles studies, J. Appl. Phys. 115 (2014), https://doi.org/10.1063/1.4861724.
[71] A. Amato, S. Terreni, M. Granata, C. Michel, B. Sassolas, L. Pinard, M. Canepa, G. Cagnoli, Observation of a correlation between internal friction and urbach energy in amorphous oxides thin films, Sci. Rep. 10 (2020) 1670, https://doi.org/10.1038/s41598-020-58380-1.
[72] J.-W. Park, S.W. Han, H.S. Moon, J.S. Lee, Effect of post-annealing on electrical properties of Ta2O5 thin film deposited by PECVD using TaCl5 and N2O, MRS online proc. Libr 309 (1993) 9–14, https://doi.org/10.1557/PROC-309-9.
[73] Y. Guo, J. Robertson, Oxygen vacancy defects in Ta2O5 showing long-range atomic re-arrangements, Appl. Phys. Lett. 104 (2014) 112906, https://doi.org/10.1063/1.4869553.
[74] R. Ramprasad, First principles study of oxygen vacancy defects in tantalum pentoxide, J. Appl. Phys. 94 (2003) 5609–5612, https://doi.org/10.1063/1.1615700.
[75] Y. Yang, H.-H. Nahm, O. Sugino, T. Ohno, Electronic structures of oxygen-deficient Ta2O5, AIP Adv. 3 (2013) 042101, https://doi.org/10.1063/1.4800899.
[76] S. Sathasivam, B.A.D. Williamson, A. Kafizas, S.A. Althabaiti, A.Y. Obaid, S. N. Basahel, D.O. Scanlon, C.J. Carmalt, I.P. Parkin, Computational and experimental study of Ta2O5 thin films, J. Phys. Chem. C. 121 (2017) 202–210, https://doi.org/10.1021/acs.jpcc.6b11073.
[77] E. Franke, C.L. Trimble, M.J. DeVries, J.A. Woollam, M. Schubert, F. Frost, Dielectric function of amorphous tantalum oxide from the far infrared to the deep

ultraviolet spectral region measured by spectroscopic ellipsometry, J. Appl. Phys. 88 (2000) 5166–5174, https://doi.org/10.1063/1.1313784.